

Characterization of on Chip CMOS-MEMS Electro-Thermal Actuator



Submitted By:

Syed Zulfiqar Haider Bukhari

[2016-MS-EE-42]

Supervisor: Dr. Farooq Ahmad

Co-Supervisor: Prof. Dr. Tahir Izhar

Department of Electrical Engineering

University of Engineering and Technology Lahore

Characterization of on Chip CMOS-MEMS Electro-Thermal Actuator

Submitted to the faculty of the Electrical Engineering Department
of the University of Engineering and Technology Lahore
in partial fulfillment of the requirements for the Degree of

Master of Science

in

Electrical Engineering

Submitted By:

Syed Zulfiqar Haider Bukhari 2016-MS-EE-42

Thesis Approved on_____

Internal Examiner

External Examiner

Chairman
Department of Electrical Engineering

Dean
Department of Electrical Engineering

Department of Electrical Engineering
University of Engineering & Technology Lahore

June-2018

Declaration

It is certified that the research work titled “*Characterization of on Chip CMOS-MEMS Electro-Thermal Actuator*” is my own work. I declare that this research work neither as a whole nor as a part has been copied from any source. The MEMS chip of Universiti Teknologi PETRONAS (UTP), Malaysia has been used for characterization in the laboratory upon their permission. It is further declared that I have developed this research work and the accompanied report entirely on the basis of our personal efforts made under the sincere guidance of my supervisor. The work has not been presented elsewhere for assessment where material has been used from other sources. It has been properly acknowledged/ referred.

Signed: _____

Date: _____

Acknowledgements

All praises and thanks to Al-Mighty “Allah”, the most merciful, the most gracious, the source of knowledge and wisdom endowed to mankind, who conferred me with the power of mind and capability to complete this thesis to the exciting ocean of knowledge. All respects are for our most beloved Holy Prophet “Muhammad (SAW)”, who is forever a torch of guidance for humanity as whole, and all the blessings that have been acknowledge below.

This research work has been carried out at the Photolithography Laboratory, Lahore University of Management Sciences (LUMS) under the kind control of Dr. Nauman Zafar Butt. Although my name appears on the cover of this dissertation, many people have contributed for successful completion of this work. I want to offer my sincere thanks to all of them.

At the very beginning, I would like to offer my cheerful thanks to Dr. Farooq Ahmad, my esteemed supervisor for preparing me as a potential M.Sc. Student, warm support and endless cooperation. I have always been extraordinary profited by his continuous help in all sort of issues, keen remarks, thoughtful comments and patience during writing up, genuinely thank you so much. I want to offer special thanks to Prof. Dr. John Ojur Dennis, Dr. M. Haris Bin Md Khir and Dr. Nor Hisham Bin Hamid whom provide the opportunity to my supervisor Dr. Farooq Ahmad to fabricate this MEMS devices at Universiti Teknologi PETRONAS (UTP), Malaysia under their kind supervision and allow me to characterize this chip also.

As a co-supervisor, Prof. Dr. Tahir Izhar supports and encourage me a lot during research work and write up. I am also thankful to him for this kindness. I am also very grateful to the pre-examiners of this research work, Dr. Farhan Mehmood and Dr. Sajid Iqbal, for their valuable comments and corrections.

Dedications

Most importantly my immediate family whom this work is dedicated to, has been a constant source of love, concern, support all the time. My parents, father Syed Muhammad Ansar Shah and my mother (late), receive my veracious gratitude, they have done more what they could, and they have dedicated their lives for us and provided unconditional love and care.

My heart-felt gratitude to my brothers and sisters for their continuous support, advice and encouragement. Special dedication to my beloved father Syed Muhammad Ansar Shah who blessed me with a lot of support. I pray to ALLAH for giving me the strength to plod on during each phase of my life.

Table of Contents

Declaration.....	iii
Acknowledgements.....	iv
Dedications.....	v
List of Figures.....	viii
List of Tables.....	ix
Abbreviations.....	x
Abstract.....	xi
Chapter 1. Introduction.....	1
1 Chapter 1.....	1
1.1 General Overview of MEMS Actuators:	1
1.2 Motivation of Research:.....	7
1.3 Scope and Limitation of Research:	8
1.4 Problem Statement:	8
1.5 Objective:.....	9
1.6 Thesis Organization:	9
Chapter 2. Literature Review.....	10
2 Chapter 2	10
2.1 Background of Electro-Thermal (ET) Actuator:.....	10
2.2 Types of Electro-Thermal (ET) Actuators:.....	13
2.2.1 U-Shaped ET Actuators:	13
2.2.2 V-Shaped ET Actuators:	15
2.2.3 Z-Shaped ET Actuator:	16
2.2.4 H-Shaped ET Actuator:.....	18
Chapter 3. Characterization Methodology.....	20
3 Chapter 3	20
3.1 CMOS-MEMS Comb Drive Electro-Thermal (ET) Actuator:	20
3.1.1 Design Parameters of CMOS-MEMS Device:	21
3.2 Device Actuation Principle:	22
3.3 Biasing of CMOS-MEMS ET Actuator:.....	23
3.4 Mechanical Modelling of Device:	25
3.4.1 Output Differential Amplitude:.....	26
3.4.2 Maximum Differential Amplitude:	27
3.4.3 Phase shift:.....	28
3.4.4 Damping Ratio:	28
3.4.5 Quality Factor:	28
3.4.6 Device Damping:	29
3.4.7 Spring Constant:.....	30
3.4.8 Resonance Frequency (fr):.....	30
3.5 Temperature of Device:	31

3.6	Experimental Setup:.....	32
3.6.1	Scanning Electron Microscopy (SEM):	32
3.6.2	Optical Characterization:	34
3.6.3	Output Force Characterization:.....	39
3.6.4	PZR as Temperature Sensor:	39
Chapter 4. Results and Discussions.....		41
4	Chapter 4.....	41
4.1	Results:.....	41
4.1.1	Input Current Vs Temperature Rise:.....	41
4.1.2	Input Current Vs Shuttle Displacement:	42
4.1.3	Input Current Vs Output Thermal Force:.....	43
4.1.4	Amplitude Vs Driving Frequency:.....	44
4.1.5	Temperature Vs Piezoresistor (PZR) Resistance:	45
4.1.6	PZR Resistance Vs Input Current Vs Temperature Rise:	46
4.2	Discussions:	47
Chapter 5. Conclusion and Future Directions.....		49
5	Chapter 5.....	49
5.1	Conclusion:	49
5.2	Future Work:	50
References.....		51
Appendix I.....		57
Appendix II.....		61

List of Figures

Figure 2.1 U-Shaped ET Actuator. (a) USA with Series Wiring (b) USA with Parallel Wiring [32].....	14
Figure 2.2 V-Shaped ET Actuator (VSA), (a) Buckle-Beam VSA , (b) Shuttle based VSA [41].....	16
Figure 2.3 Z-Shaped ET Actuator (ZSA) [34].....	17
Figure 2.4 H-Shaped ET Actuator (HSA) [19].....	18
Figure 3.1 Central Shuttle based Comb Drive Electro-Thermal (ET) Actuator [39] ..	22
Figure 3.2 (a) Resonating Comb Drive Electro-Thermal (ET) Actuator, (b) Cross Sectional View of Long Beams, (c) Cross Sectional Layers Scheme of Central Shuttle [38].....	24
Figure 3.3 FESEM Image of CMOS-MEMS Electro-Thermal (ET) Actuator [43]....	33
Figure 3.4 Front View of Multi Project Wafer (MPW) Die	33
Figure 3.5 (a) Front Side View of JIG (b) Back Side View of JIG	34
Figure 3.6 The Dual Inline Package (DIP) Placed into JIG.....	35
Figure 3.7 The Original CMOS-MEMS ET Actuator Chip Placed Under Dual Inline Package (DIP)	35
Figure 3.8 Wire Bonding of CMOS-MEMS Chip.....	36
Figure 3.9 The Pad Configuration with CMOS-MEMS ET Actuator Chip [45].....	37
Figure 3.10 Optical Characterization Setup for Static Mode Measurements	37
Figure 3.11 Optical Characterization Setup for Resonant Frequency Mode Measurements	38
Figure 3.12 Experimental Setup for PZR Resistance Measurement.....	39
Figure 4.1 Input Current Vs Temperature Change in CMOS-MEMS ET Chip	41
Figure 4.2 Central Shuttle Displacement Measurement in Static Mode.....	42
Figure 4.3 Input Current Vs Displacement Produced in Central Shuttle.....	43
Figure 4.4 Input Current Vs Thermal Force Produced in Central Shuttle.....	43
Figure 4.5 Amplitude Measurement at Resonance Frequency	44
Figure 4.6 Amplitude Vs Driving Frequency in Dynamic Mode	45
Figure 4.7 Central Shuttle Temperature Vs Resistance Changes in PZR.....	46
Figure 4.8 Resistance Change in PZR Vs Input Current Vs Temperature Changes in Central Shuttle	46

List of Tables

Table 2.1 Comparison among different MEMS ET Actuators	19
Table 3.1 Material Properties of CMOS-MEMS ET Actuator	21
Table 3.2 Design Parameters of Resonating Comb Drive ET Actuator	22
Table 3.3 DIP Vs Chip Pads Connections.....	36
Table 3.4 Chip Pad Connections with CMOS-MEMS Device.....	36
Table 4.1 Comparison between Experimental and Theoretical Analysis	47

Abbreviations

MEMS	Micro-electro-mechanical System
CMOS	Complementary Metal Oxide Semiconductor
IC	Integrated Circuit
ET Actuator	Electrothermal Actuator
USA	U-Shaped Actuator
VSA	V-Shaped Actuator
ZSA	Z-Shaped Actuator
HSA	H-Shaped Actuator
PZR	Piezoresistor
SEM	Scanning Electron Microscopy
DRIE	Deep Reactive Ion Etching
MetalMUMP	Metal Multi User MEMS Process
PolyMUMP	Poly Multi User MEMS Process
SOI-MUMP	Silicon On Insulator Multi User MEMS Process
VOA	Variable Optical Attenuator
MPW	Multi Project Wafer
TCR	Temperature Coefficient of Resistance
TEC	Thermal Expansion Coefficient
LIGA	Lithographie Galvanoformung Abformung
DIP	Dual Inline Package
LCD	Liquid Crystal Display
MIMOS	Malaysian Institute of Microelectronic Systems

Abstract

The Electro-Thermal (ET) MEMS actuators are playing an important role in Micro-Electro-Mechanical System (MEMS) technology due to its high efficiency. The characterization of MEMS ET actuator is presented in this research work. This actuator chip had been fabricated using 0.35 μm Complementary Metal Oxide Semiconductor (CMOS) and released to pack in Dual Inline package (DIP). The thermal force based CMOS-MEMS micro actuator consists of central shuttle and four supporting long beams. The central shuttle resonates in lateral mode (1st mode of direction) in the consequence of AC biasing through four long beams. The polysilicon peizoresistors (PZR) are also embedded along the four beams which have been used as temperature sensor. In the presence of thermal force, the actuator has been actuated to produce the maximum amplitude at resonance and recorded that ET micro actuators provide maximum amplitude. The amplitude, resonance frequency, damping ratio, quality factor, thermal force and driving voltages are characterized by optical characterization method and finally compared to theoretical measurements. The differential change in amplitude at different driving frequency have been determined by optical characterization and compared to theoretical measurements. The maximum amplitude, resonance frequency, bandwidth, quality factor, damping ratio and thermal force has been measured 71.15 μm , 8596Hz, 295.74Hz, 29.16, 0.0171 and 6.68 μN theoretically, while the experimental measurements have been found to be 74.7 μm , 8570Hz, 285Hz, 30.07, 0.0170 and 6.75 μN respectively. Further, calibration curve of the temperature sensor is plotted theoretically and compared to the experimental results to found the sensitivity in terms of change in resistance per degree ($\Omega/^\circ\text{C}$). The sensitivity due to change in temperature has been observed with the help of change in resistance of PZR embedded on the long beams of MEMS ET Actuator. The sensitivity is measured approximately 355m $\Omega/^\circ\text{C}$ theoretically and 356m $\Omega/^\circ\text{C}$ experimentally.

Chapter 1

Introduction

1.1 General Overview of MEMS Actuators:

Everyday life of science & technology depends upon various sensing and actuation mechanisms to perform some action or changes. These various mechanisms are required to bring some huge level changes in the systems such as in biological field, chemical, electronics, telecommunication, RADAR communication, satellite communication, wireless & mobile communication, optical communication, automotive, computer, biomedical fields, navigation systems, aerodynamics, aircrafts and agriculture field etc. These mechanisms have been successfully performed on the existing technologies on the basis of various principles of sensing and actuation. The old technologies require high power consumption, huge actuation device size and high cost which provide meaningless performance and sensitivity [1]. Sensor is used to sense changes in a system while actuator produce actuation accordingly to control system effectively and efficiently. Actuators are generally used to produce displacement, mechanical motion, force or torque. The researcher devoted to improve the performance and sensitivity under relatively low power consumption, compact sensor or actuator size with low cost. They tried to reduce the geometric parameters of sensing and actuation device to improve the above constraints. They reduce their parameters so that they successfully reached down to micron or nanometer scaled sensors and actuators. The micrometer actuators are very important to use for same purpose as bulky size actuator have been used. These tiny devices are also used for sensing and actuation mechanisms same as above. These micron size devices has developed the concept of MEMS.

The Micro-Electro-Mechanical-System (MEMS) consists of mechanical components such as sensors and actuators along with electronic components on the substrate. The integration of mechanical and electronic elements is performed using micro fabrication technology on the substrate. The MEMS devices facilitate the user such as availability at low cost with reduced size at low power consumption and need

few voltages to operate etc [2]. The MEMS devices can be further categorized into two major classes. First one is the sensors and second one is the actuators. Sensor is a device in which some input transduces in mechanical domain (i.e. physical and chemical phenomenon) and output perception in electrical domain (i.e. electrical signals) [3].

In the development of MEMS, micro actuators are very important part which are used for driving mechanism. Broadly speaking, actuation at micron level is energy transduction processes and produce some action. In other words, actuators in MEMS are the devices which are used to produce force or displacement via some suitable method to transform electrical energy to mechanical energy [4]. Actuators are used in micro grippers [5][6], micro mirrors [7][8], micro pumps [9], micro switches [10], and optical switches etc. In actuators, micro-cantilever is a basic structure and tip deflection at the other end is used for actuation purpose. There are several mechanism to actuate the actuators like piezoelectric, electro-magnetic, electrostatic and electro-thermal actuators [11].

The piezoelectric actuation is performed, when electric field is used to induce strain in the material which produces displacement. In piezoelectric actuation, an electric field is applied across the piezoelectric material, a strain is produced in the material which leads to produce displacement and force. Piezoelectric actuation provides fast switching speed and high output force at low driving voltages. These actuator produces some useful displacement if even small amount of deformation is produced in the material. Although its fabrication is more complex but it offers high gripping force at low stroke. The stroke can be increased by amplification mechanism of piezoelectric devices. It can also use for sensing mechanism as well as actuation mechanism simultaneously.

Electromagnetic actuation mechanism require some sort of special material in micro fabrication process to actuate the device electromagnetically. When the electric current pass through the current carrying material in the presence of varying external magnetic field. A Lorentz force is generated perpendicular to the direction of current flowing which used to actuate the actuator's cantilever to produce displacement. This actuation mechanism provide fast switching speed, high output force, low power of operation at few driving voltages. It can also use for sensing and actuation mechanism similarly. It is not so simple to fabricate the electromagnetic actuator as compare to the electrostatic and Electro-Thermal (ET) actuator.

In MEMS, electrostatic micro actuator is the device which is used to study output force, displacement and voltage. The electrostatic force is produced between the two electrodes, when different electric potential is applied between two parallel plates which are placed at some specific dielectric gap. This electrostatic force pulls the one moving plate towards the fixed plate of the actuator which produces displacement. This micro actuator usually provides comparatively small output forces, displacements and high operating voltages [12]. This micro actuator has typically small deflections either require high driving voltage for large deflections. This actuator is usually more desirable because it operates at high frequency and low output power. This actuation mechanism offers large chip area, highest frequency response, low power consumption with low output force. It is simple to fabricate the micro actuator as compared to the piezoelectric and electromagnetic actuator. It is also used for sensing and actuation mechanism simultaneously like piezoelectric and electromagnetic actuator.

The electro-thermal (ET) micro actuation mechanism is one of the most important actuation mechanisms which offers low driving/operating voltage with maximum displacement/amplitude and produces high output force. When the electric current is applied to the material, the thermal expansion is produced due to a rise in temperature in the material according to the Joule heating effect principle [13]. The ET micro actuator provides large perpendicular or parallel deflections to the substrate output force. It has more robustness as compared to the electrostatic actuator. Its fabrication is also simple as compared to the piezoelectric and electromagnetic actuators. A valuable complement shows the ET actuator to the electrostatics actuator. It cannot be used for parallel actuation as well as sensing mechanisms as compared to the other micro actuator.

There are two major categories of electrothermal (ET) micro actuators according to the direction of motion. One is the in-plane ET actuators [14] and the other is out-of-plane ET actuators [15]. In-plane ET actuators are fabricated using surface micromachining process because it is easy to fabricate it in this fabrication process. Out-of-plane ET actuators are fabricated using bulk micromachining process which is complex to the previous one. Bulk micromachining process is a more effective method for out-of-plane ET actuator. Therefore, out of plane ET actuators are usually used instead of in plane electro-thermal actuators.

The U-shaped [16], V-shaped [17], Z-shaped [18] and H-shaped [19] electro thermal (ET) actuators are the basic four types of actuators according to the shapes of ET actuator. Their detail is described in chapter 2. All these actuators operates according to the joule heating effect principle. These ET actuators are fabricated using various technology such as metalMUMPs, polyMUMPs, SOI-MUMPs and CMOS etc.

The MetalMUMPs technology has been used to fabricate the ET micro actuators which is provided by MEMSCAP Inc. The MUMPs is abbreviated from Multi-User MEMS Processes which is standardized MEMS process. The MetalMUMPs is used for to perform several projects on the single wafer for the manufacturing of volume. So the cost has been shared on each project performed on that single wafer. Therefore researcher found it as cost effective fabrication process with good reliabilities. There were found drawback of standardization for all user in this process. It cannot not provide the customized flexible steps to complete the process for single project. The researchers has to bear the additional cost even to complete single project [6].

In early, ET micro actuators are also fabricated using PolyMUMPs process. The PolyMUMPs is abbreviated from Poly Multi-User MEMS Processes. This process is used for surface micromachining process in which the three polysilicon layers are used. This is commercially used for fabrication because this is proof of concepts to the universities, industries, and government worldwide. The cost effective is the most important factor for it's commercially use fabrication technology of ET micro actuator. In this process polysilicon is used as structural layer, the deposited oxide is used as sacrificial layer and silicon nitride layer is used between polysilicon and substrate as electrical isolation [16].

The SOI-MUMPs is used for the fabrication of MEMS variable optical attenuator based on the Electro-Thermal (ET) micro actuators. The SOI-MUMPs is abbreviated from Silicon On Insulator Multi-User MEMS Processes. The silicon on wafer is used to start the process. It is simple 4-level mask process for etching and patterning. We can obtain the oxide layer by etching down to the doped Silicon and patterned layer in this process. The patterned substrate is etched through the bottom side of the wafer to reach at oxide layer. The pad metal is made by the first deposited layer. The second mask level is patterned with silicon lithographically. A protection layer is also applied on the top surface of the silicon layer [20].

CMOS is abbreviated from complementary metal oxide semiconductor. CMOS technology is one of the most important technology in the modern research of MEMS devices fabrication. It is the technology for integrated circuits (IC) construction and used as commercially in MEMS ET actuator fabrication. A typical layout is designed of the device in first step of CMOS fabrication technology. The MEMS component layout is patterned by CMOS layer. Then etching process is done to release the MEMS ET structure from the movable parts. After this, the CMOS circuit can be integrated on the layer of MEMS devices during fabrication process. The main advantage of CMOS technology is to use low power consumption, small size, reduced cost, improved yield, improved performance, improved value and highly immune to noise [3]. CMOS compatible approach with MEMS devices allows higher performance with small size of device. Another top layer is used to protect entirely the CMOS circuitry which layer is used as mask layer to define MEMS structure during post micromachining process. The integration of CMOS technology with MEMS technology is known as CMOS-MEMS technology. Therefore this process is known as CMOS compatible process [21]. Due to multi-metal layers, IC (integrated circuits) facilitated by the wiring of MEMS structures in CMOS-MEMS technology. The achievement of high performance device and the reduction of parasitic capacitance of CMOS-MEMS devices can be obtained via monolithic integration. But the CMOS technology limits the MEMS design structure due to its difficulty. The comparison of CMOS technology to the different MUMPs is briefly demonstrated in table 1.1.

CMOS-MEMS Electro-Thermal (ET) actuation characteristics has been described in terms of resonance frequency, voltage requirement, force, maximum deflection (displacement)/ amplitude and sensitivity of the device [4]. Numerous industrial applications has been applied by this type of thermal actuation device such as in micro robotics, flying robotics , micro drones, micro-mirrors, micro switches, optical switches [22], micro grippers, variable optical attenuator, micro testing device, micro pumps, biomedical applications and many RF applications. It is also used in many other industrial applications such as injekt printers, dj printers, airbags, automation, embedded systems, switching systems, robotics, variable optical attenuators (VOA) aircraft, navigation systems, whether investigation systems and many other telecommunication systems such as radar and satellite communication systems, optical communication systems, and optical switches. In short, ET actuators

have comprehensive scope in sense of application industrially and commercially. The ET micro actuator is used in many applications which not only provide high output force, large amplitude or displacement and low driving voltages but it also provide better sensitivity. Besides these wide range of CMOS-MEMS ET actuator applications or advantages, there have been investigated some limitation in this type of MEMS actuation device. The CMOS-MEMS ET micro actuator has slow speed, or less tuning and provide less efficiency in quick actions as compared to MEMS electrostatic actuation device. Therefore it is limited to fast switching purposes. It is used where slow switching mechanism is needed. We have to compromise with its some applications due to high operating chip temperature which is not appropriately for biological samples handling typically. The maximum bandwidth range of ET actuator is in kilohertz (kHz). The CMOS-MEMS ET micro actuator require more power to consume in milli-watts range at ambient temperature sensitivity, as compare electrostatic actuators [4]. Therefore this micro actuator is limited where the low power consumption mechanism is required.

But in this research work, we have investigated a new type CMOS-MEMS electro thermal (ET) actuator which is known as central shuttle based Comb drive ET actuator [23]. This actuator is based on V-shaped and Z-shaped thermal micro actuator. It is some sort of extended form of V-shaped and Z-shaped ET micro actuator. This ET micro actuators is also work on the principle of joule heating effect like other ET micro actuators. The characterization of CMOS based MEMS Electro-Thermal (ET) micro actuator which has been fabricated using 0.35 μ m CMOS technology, is presented in this research. The characterization is described in terms of resonance frequency, voltage requirement, force, quality factor and damping ratio, maximum deflection (displacement) and maximum amplitude and sensitivity of the device. It is also used in micro-mirrors, micro switches, optical switches, micro grippers, variable optical attenuator, micro testing device, micro pumps, biomedical applications and many RF applications. Further, they are also used in micro robotics [24], and flying robotics i.e in micro drones etc. The ET micro actuator is also used in many applications which provide high output force, large amplitude displacement and low driving voltages. In the past, some thermal actuators are designed for micro grippers, micro mirrors, micro pumps and biomedical applications, although that are easy to integrate with electronics and low cost for batch fabrication but constrained to poor actuation mechanism with comparatively large driving voltage, power

consumption, low amplitudes and force. But our proposed device in this research work, is design to overcome these limitations in the electro thermal (ET) actuator applications. COMS-MEMS comb drive ET micro actuator is fabricated by the post micromachining process. The post micromachining technique has two sub fabrication techniques as described in [4]. One is thin film Post-CMOS MEMS technology [21] and other is Deep Reactive Ion Etching (DRIE) post-CMOS MEMS technology [25]. The comb drive resonating ET actuator was fabricated by using DRIE post CMOS-MEMS technology process.

1.2 Motivation of Research:

In previous technologies, heavy weighted, bulky size sensing and actuation devices have been used in various fields. The conventional actuators have been used whose geometric parameters were designed at large scale (i.e. centimeter or meter range). These previous technology based actuator devices require lot of power consumption to operate. These actuators need high capital investment to produce even a small amount force and small amplitude or displacement to use for the specific actuation application. These old technology based heavy weighed, bulky size, large power consuming, high cost effective actuators provide poor performance in form of small amplitude or deflection, low forces, slow speed, and require more driving voltages to operate. All these deficiencies motivated the researchers to improve its performance by varying its geometric parameters in such a way that all the specific field applications of the actuator may meet its requirements with excellent performance. So the researchers devoted to miniaturize the scale of sensors and actuators. The miniaturization has been done down to millimeter scale and forward to micrometer scale to evaluate the performance of the devices with reduced size. These micrometer scale electro mechanical actuator devices integrated with electronic components refers to MEMS actuator. These miniaturized MEMS actuators provide exceptional performance in every aspects such as small size (micro scale), light weight, low power consumption, cheap cost which provide maximum deflection amplitude, appropriate output power, fast speed and require very few voltages to operate. These developed MEMS actuators use for its specific applications of actuations such as MEMS electro-thermal (ET) actuators are used in tiny devices i.e microgrippers, micromirrors, micropumps, variable optical attenuators, inject printers, dj printers, airbags and biomedical equipment etc. These micrometer level devices

produce incomparable performance to millimeter, centimeter meter level scale devices. One of the other major advantage is the use of monolithic integration in such micro scale devices. The word monolithic refers to one stone. The fabrication of various component on a single substrate is known as monolithic fabrication. In monolithic integration, Single wafer is used for integration of electronic processor or controller with mechanical actuator. This motivated phenomena is very important to improve the signal quality by the reduction of signal path length in MEMS actuator devices. Now the MEMS devices growing commercially in the markets. Because small scale devices dedicated to use in advance machinery in the industry to achieve excellent performance with greater sensitivity at low cost. A lot of industrial applications has been developed by MEMS actuation mechanism due their high performance achievement with greater sensitivity and controllability.

1.3 Scope and Limitation of Research:

MEMS based actuators have been studied with detail in this research work. The various MEMS based ET actuators have been describes to evaluate their performance in this research work. Among the MEMS ET actuators, comb drive CMOS-MEMS ET actuator chip is characterized to investigate its performance here. This chip has been fabricated using 0.35 μ m technology in MIMOS Bhd Company (Kuala Lumpur, Malaysia) with the collaboration of Universiti Teknologi PETRONAS (UTP), Malaysia. The characterization of CMOS-MEMS ET micro actuator has been done in terms of resonance frequency, damping ratio, damping constant, damping coefficient, voltage requirement, output thermal force, maximum displacement (deflection) or amplitude, quality factor, change in piezoresistor (PZR) resistance behavior due to change in temperature of chip and sensitivity in this research. I have realized its overall performance, output force characterization, sensitivity and its applications to find that it has some improvements from older ones and reported in this thesis with detail.

1.4 Problem Statement:

MEMS Electro-Thermal (ET) actuators are used in many electronic and biomedical applications. V-Shaped, U-shaped, H-shaped and Z-shaped actuators are the various type of MEMS ET micro actuators which have been fabricated, tested and characterized through various technologies. All of them micro actuators have problems which can be considered for further research. One of the common problem

is that all ET actuators use to operate comparatively high driving voltages as described in [26]. In the previous research work, high driving voltages (i.e. 10V) are applied to get 135 μ m displacement [26]. This high driving voltage problem is considered to improve the results to obtain the maximum displacement or amplitude at low driving voltage in this research work.

The characterization of comb drive electro thermal (ET) micro actuator is presented in this research work which was fabricated using 0.35 μ m CMOS technology to overcome the high driving voltages problems and to provide good performance like high displacement or amplitude, force and less power requirement to cover more angle in micro-mirrors, micro pumps and optical switches and have low design cost and reliable for monolithic integration.

1.5 Objective:

The objective of this research work is to characterize CMOS based comb drive MEMS ET actuator which was fabricated using 0.35 μ m technology to evaluate:

- Output amplitude of ET actuator at low driving voltages.
- Output force of ET actuator.
- Quality factor of micro actuator.

1.6 Thesis Organization:

In this research work, the Optical characterization method is proposed for the characterization of CMOS-MEMS ET actuator. The measurements of this proposed optical characterization method compared to the theoretical measurements. The thesis organization is given below:

- **Chapter 1** describes the general overview of the MEMS actuators, motivation, scope and limitation of research, problem statement and objective of research is briefly explained.
- **Chapter 2** describes the explanation of ET actuator background, ET actuation mechanism, ET types and its working principle.
- **Chapter 3** describes the characterization methodology, mechanical modelling, experimental laboratory setup and working.
- **Chapter 4** describes the experimental results which are compared to the theoretical results and discussed.
- **Chapter 5** describes the conclusion and future directions of this research work.

Chapter 2

Literature Review

2.1 Background of Electro-Thermal (ET) Actuator:

In microsystem or MEMS, micro actuators are devices that are used to produce displacement and force by the transduction of some input in electrical domain which are typically transform to mechanical domain as an output of the actuators via changes in intermediate energy domains either directly or indirectly. MEMS actuators are used to convert energy into some proper action which is accomplish for generating some motion in micro scale for individual elements positioning.

MEMS micro actuators are classified into four different classes according to different principles. Piezoelectric, electro-magnetic, electro-static and electro-thermal micro actuator are these four main classes [4]. Some special material is mandatory for the complication of micro fabrication process for piezoelectric and electromagnetic actuator. Electrostatic actuator provide the small range of controllable displacement and less functional robustness. Electro-thermal actuator can provide large output force, stable and controllable amplitude (displacement). ET actuators have standard Integrated circuit (IC) micro-fabrication process compatibility as well as material. Among the other actuators, MEMS thermal actuators usually used polycrystalline silicon material either heat generating source in metal based thermal actuators or to fabricate the thermal actuators which are poly silicon based. In some cases, as the temperature profile of thermal actuator changes, the poly silicon resistivity also changes. Therefore it is essential for poly-silicon resistivity characterization to realize the ET actuator behavior or to improve more precise model [27].

Judy *et al.* introduced the first in-place MEMS electro thermal micro actuator using high resistance poly silicon beams which encompassing serpentine microbridge and alternately coated with platinum. “Hot-arm” actuator, “heatuator”, “pseudobimorph” or “U-shaped” actuator topology demonstrated by Guckel *et al.* which was fabricated using a sacrificial LIGA (lithographie- galvanoformung-

abformung) process in nickel. The actuators which fabricated by poly silicon with double hot-arms topology to enhanced the efficiency of the actuator was described by Comtois *et al.* in which the temperature difference was increased between cold and hot-arm by the removal of cold-arm from electrical current path. “V-shaped”, “chevron,” or “bent-been” Electro thermal actuator topology first demonstrated by Noworolski *et al.* This topology was originated for the sensor which use as passive strain by Najafi and Gianchandani *et al.* Recently, Single and cascaded bent-beam actuators topology also reported by Que *et al.* Thermal expansion principle based U-shaped electro thermal poly silicon actuator with thin or thick arm developed by Tichem, Henneken and Sarro *et al.* Thermal expansion based principle micro cantilever ET actuator consist of single material. Differential of thermal expansion principle in only applied for multilayer ET actuator. Multilayer ET actuator (two layer ET actuator) with thickness of optimum layer was reported by Hsu, Cheng, Lai and Chan *et al.* Electro thermal analytical three layer micro actuator modeling was investigated by Hilleringmann, shui and Jiang *et al.* Downward and upward bending of bi-material was reported by Hsu, Huang, Chung and Cheng *et al* [4].

The actuators which are widely used in MEMS actuation mechanism, are electrostatic and electro thermal actuators. These two classes of actuators have very different characteristics although these actuators have same basic electrical energy utilizing functions to produce output force and displacement. The electrostatic based micro actuators have typically small deflections either require high driving voltage for large deflections or dimensional tolerances closed. These actuators are usually more desirable because they operate at high frequency and low output power [25]. On other end, actuators which are based on thermal expansion have advantage of large driving output force and large displacement with very low driving voltage. The electro thermal micro actuators provides large perpendicular or parallel deflections to the substrate output force [28]. A valuable complement shows the ET actuator to the electrostatics actuator. The fabrication of these actuators have been done by post-CMOS micromachining. The post-CMOS micromachining is a process in which foundry CMOS silicon substrate interconnect and interlayer dielectric act as structural material in MEMS.

As we compared to the electrostatic micro actuators, electro-thermal (ET) actuators are less efficient in quick actions and limited in some applications like micro

biological samples handling. Actually the dynamic design of this actuator is the main cause behind this deficiency. In previous research of this ET actuator, U-shaped ET actuator mechanical modeling addressed which dynamically designed. The behavior of U-shaped ET actuator was dynamic and the response of thermal mechanical modeling was as quasi-static. There is no accurate analysis and analytical modeling has been described in which the dynamically response addressed of V-shaped and Z-shaped ET actuators according to the authors [29]. Therefore static level leads to accuracy in design of dimension parameters and the behavior of V-shaped and Z-Shaped ET actuator. Micro actuators fall into two different types which are in-plane and out-of-plane according to different motion forms. Further, all these ET actuators works on the basis of joule heating effect principle of material thermal expansion.

The principle describes that when voltage is applied across the some resistive material in the presence of temperature coefficient of resistance (TCR). Heat is generated in metal material (i.e. polysilicon, aluminum and silicon dioxide in CMOS-MEMS devices) when the current pass through this material. The temperature coefficient of resistance (TCR) increases due to the high current density in the metal. So, the thermal energy stored in the material. The material resists the raise of temperature produced in the material. As the temperature raise at the consequence of continuously applied voltage and current, the material expands according to its thermal expansion coefficient (TEC) its self so that the material thermal energy and temperature may sustain in the same material. Therefore, electrical energy is converted into thermal energy which finally converted into mechanical energy. The material having high thermal expansion coefficient (TEC) value expands more than the material having low TEC value. As a result, thermal expansion is produced due the thermal expansion is thin material [30]. This thermal expansion causes elongation in the beams of the thermal actuators which is known as displacement or amplitude.

My research in this thesis work is on new type of electro-thermal (ET) actuator which is known as comb drive ET actuator. The long beams of this actuators are made of aluminum and polysilicon with alternatively used silicon dioxide among each layer in structure. Comb drive ET actuator is an important type of actuator whose fabrication, design and implementation is easy as compared to other electro thermal actuators. It has been used in different fields of applications such as nanotechnology, optical communication, wireless communication and biomedical

engineering. There are two main concerns for the development of comb drive ET actuator in which first one is large output force and second one is long travelling distance. These two main performance features were used for the improvement and devotion of many researcher's efforts from last two plus decades. These researcher's efforts may fall into four major categories which are spring shape modification, finger shape optimization, finger overlaps configuration and modification and methods of creating new actuation [23].

There are many demerits of ordinary electro thermal actuators which include sensitivity to fluctuation of ambient temperature, bandwidth of maximum range in KHz and power consumption about 1-20mW range. Further high driving voltages related problems are also major concerns as drawbacks of electro-thermal (ET) actuators. But in this research work, our major concern is to characterize the comb drive CMOS based MEMS electro-thermal (ET) micro actuator which have been fabricated using 0.35 μ m CMOS dry post micromachining technology, for high displacement at low driving voltage under appropriate power consumption and power delivered.

2.2 Types of Electro-Thermal (ET) Actuators:

There are many types ET actuators but the U-shaped, V-shaped, Z-shaped and H-shaped ET actuators are basic types which are described as follows. The CMOS-MEMS comb-drive ET actuation mechanism is an extension of V-shaped and Z-shaped ET actuators which is described in detail in chapter 3.

2.2.1 U-Shaped ET Actuators:

U-Shaped actuator (USA) is also known as pseudo bi-morph actuator. Pseudo bi-morph actuator consist of cold and hot arms associated with anchors. Cold arm is usually wider than the hot arm. These arms are joined together at the other end. USA operates on the principle of joule heating effect in which the poly-silicon material thermally expands when the electric current pass through the actuators via anchors. When the voltage difference is applied to the anchors of USA. The more heat is produced in narrow hot arm than cold arm. The more current density is produced due to the more resistance of the heat in narrow arm [31]. In the consequence of temperature increment in the hot arm due to more current density, arm extends which produce motion the in the actuator. The large displacements and high forces (few

micro newton) are achieved by the CMOS compatible voltages and currents by this type of actuator.

However, same material is used in narrow and wide arm of the actuator. Therefore the thermal expansion coefficient of the actuator is also same. Hence the temperature difference generated in the hot and cold arm which is the main reason to actuate the U-shaped ET actuator. Because the hot arm of the USA is thinner than the cold arm, more current resistance exists in the hot arm. The more heat is generated which leads to some extension in the hot arm. Therefore displacement is produced due to the thermal expansion of the hot arm. As a result, USA bends towards the cold arm. Therefore this displacement is circular as an arc shape. U-shaped ET actuator can produce displacement on both directions i.e. either towards cold arm or towards hot arm. When you require to move it towards cold arm, you need to apply voltage difference in series configuration of the anchors. But when you require to move is towards hot arm, you need to apply voltage difference in parallel configuration of the anchors as shown in fig.2.1. Therefore USA is usually used for bi-direction displacement purposes [32].

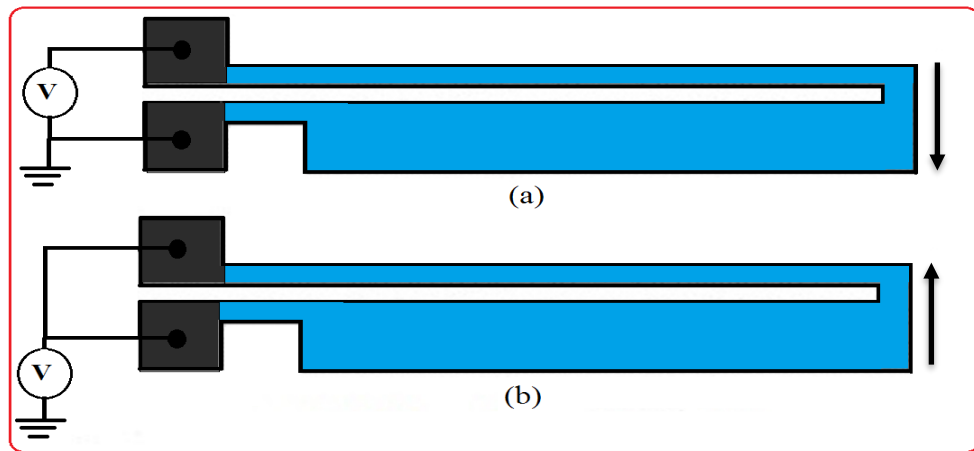


Figure 2.1 U-Shaped ET Actuator. (a) USA with Series Wiring (b) USA with Parallel Wiring [32]

There are many other advantages rather than large displacement and high output force of this type of actuators. These typical actuators require small footprint size and used for micro-gripping, micro-position, manipulations and many other micro-scale and nano-scale applications. The typical order of lateral displacement of USA is some μm . The lateral displacement is typically proportional to the thermal expansion of the material. The small deflection is generally equal to thermal expansion of the material multiplied by the length of the actuator and divided by separation of cold and hot arms [33]. The Operating Voltages of such type of

actuators depends on its geometry but the typical range of operating voltage of USA is from 0 to 14 volts and current range from 0 to 5 mA which is standard CMOS compatible voltage and current regimes. The displacement is proportional to square of applied voltage (V^2). A typical CMOS-MEMS USA actuator whose length 200 micron can provide 16 micron deflection and produce 13 micro newton (μN) force usually.

2.2.2 V-Shaped ET Actuators:

V-shaped actuator (VSA) is also known as chevron electro-thermal (ET) actuator. Chevron ET actuator consist of two hot beams (hot arms) connected with anchors at free end where the voltage is applied. These two hot beams either directly connected to each other with small angle θ or connected to central shuttle and known as chevron or V-shaped ET actuator. The central shuttle has polysilicon resistance in it. The directly connected hot beams structure is also known as buckle-beam actuator as shown in fig.2.2 (a). A typical shuttle based V-shaped ET actuator is shown in fig.2.2 (b). VSA is usually fabricated by bimorph polysilicon and silicon dioxide material using post-CMOS micromachining technology. The metal inter-connect to the dielectric inter-layer and CMOS foundry silicon substrate in post-CMOS micromachining technology. The shuttle based comb-finger chip (field of interest in this research work) which is going to characterize its ET actuation, is also the extension of V-shaped ET actuator. The shuttle based comb-finger MEMS device is also fabricated by DRIE post CMOS-MEMS technology. The detail description of this MEMS device is given in chapter 3. However when the voltage is applied to the anchors of the VSA, current pass through hot beams. Therefore high temperature is generated due to high current density in both narrow beams. These narrow hot beams extend in its length due to production of high temperature. The compatible voltage and current with standard IC (CMOS) are applied to operate the actuator by the polysilicon resistivity. As a result, some motion is produce in central shuttle this produced displacement is due to this thermal expansion in the actuator [33].

A typical VSA produce the thermal expansion on the order of $0.2\mu\text{m}$ to $0.3\mu\text{m}$ for angle $\theta=6^\circ$. VSA produce typically large displacement at small angles as compared to the USA. The displacement is approximately 10 times larger than the USA and the thermal expansion produce up to few microns. The comparatively low operating voltage is used to actuate this type of actuator and operating voltage depends on its

geometry. But at the high temperature, buckle-beams limits its maximum displacement as in pseudo bimorph actuator. However VSA maximum displacement is also proportional to square of applied voltage (V^2) as same as in USA.

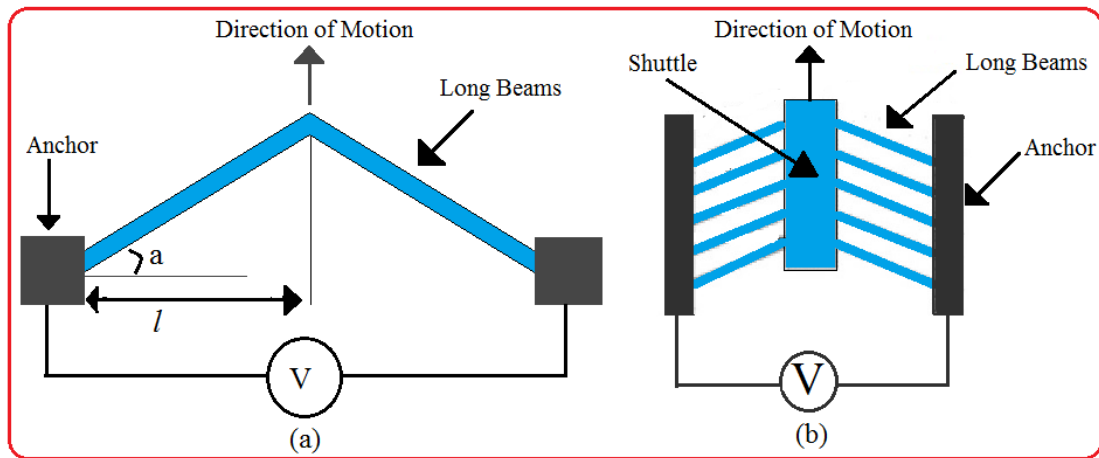


Figure 2.2 V-Shaped ET Actuator (VSA), (a) Buckle-Beam VSA , (b) Shuttle based VSA [41]

A single V-shaped thermal actuator produce less deflection and more output force as compared to the U-shaped thermal actuator but it produce large deflections and output force (compared to the Single VSA) when multiple hot arms pairs are used in parallel orientation. The V-shaped thermal actuator is more efficient than the U-shaped thermal actuator due the absence of the cold arm which limits the thermal expansion. There are various advantage of V-shaped thermal actuator. Large stiffness, small feature size, comparatively low operating voltage, maximum displacement, high output force (few mN) are major advantages of this type of actuator. VSA produce perfect controllable displacement due to the huge stiffness in the actuator. But no more than few μm range displacement is produced and the high output force (order of mN) can easily be generated by this type of actuator. VSA cannot be simultaneously used as sensor and actuator as compared to the electrostatic devices. Therefore there is need for extra sensor for the application of nano-manufacturing and nano-mechanical testing purposes [27].

2.2.3 Z-Shaped ET Actuator:

Z-shaped Actuator (ZSA) is similar in structure to the V-shaped actuator (VSA) but there is small difference in the beams of the both actuators [29]. The narrow beams (hot arms) are symmetric to Z shape. The both Z shape beams are connected to the anchors of the actuator at the free end but these two beams are connected to the central shuttle. The Z shape beams are further divided into long

beams (denoted by L) which is horizontal part of the beams and short beams (denoted by l) which is vertical part of the beams [18]. The Typical Z-shaped actuator (ZSA) is shown in fig. 2.3.

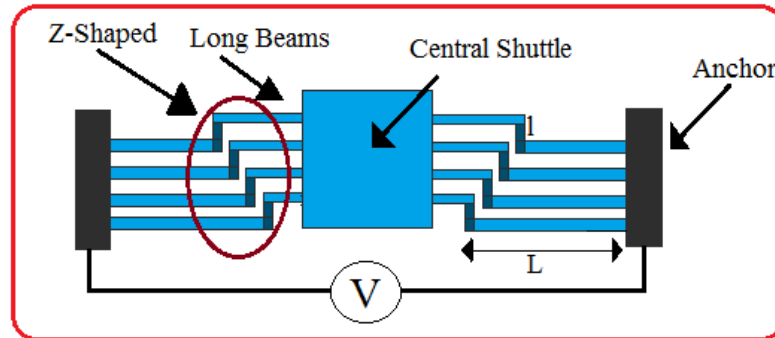


Figure 2.3 Z-Shaped ET Actuator (ZSA) [34]

The central shuttle has bimorph polysilicon resistance in it. ZSA is usually fabricated by bimorph polysilicon and silicon dioxide material using post-CMOS micromachining technology. The metal inter-connect to the dielectric inter-layer and CMOS foundry silicon substrate in post-CMOS micromachining technology. When the voltage is applied to the anchors of the ZSA, high temperature is generated due to high current density in both narrow Z shape beams according to joule heating effect. These hot arm or Z shape beams extend in its length due to production of high temperature especially in long beams (whose length denoted by L). Due to symmetry in the beams length, long beams (L) do not extend. The extension of long beams length accommodates to the short beams (whose length denoted by l) which is vertical part of the beams. This is the thermal expansion of the beam due high temperature inducement. As a result central shuttle motion is achieved due to net elongation of the Z shape beams [34]. Therefore, rectilinear displacement is achieved by this type of actuator as similar to V-shape thermal actuator. The compatible voltage and current with standard IC (CMOS) are applied to operate the shuttle of actuator by the polysilicon resistivity.

Z-shaped thermal actuator overcome the shortcomings of V-shaped thermal actuator. The large displacement and high output force is achieved as compare to V-shape thermal actuator due to the high stiffness. The large displacement is easily achieved and the high output force is comparatively difficult to achieve as compare to the VSA. But it is complementary of the comb drive for large range of stiffness and high output force as in ZSA [35].

2.2.4 H-Shaped ET Actuator:

H-shaped actuator (HSA) consists of two long beams, four anchors and one link beam. Each long beams are connected with two anchors on both sides of the beams and the link beam is connected to middle position of two long beams to make H shape. Therefore these four anchors which are used as electrical pads, are located on the four corners of the actuator. A typical H-shape actuator is shown in fig.2.4.

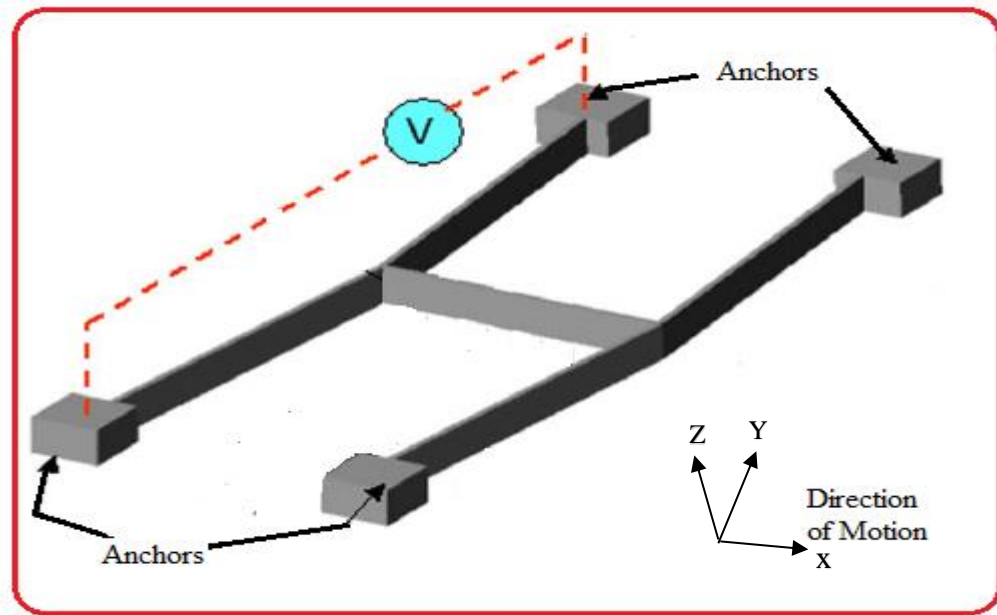


Figure 2.4 H-Shaped ET Actuator (HSA) [19]

Each anchor is made by silicon Si material and beams are made by bimorph polysilicon and silicon dioxide materials which are fabricated by post-CMOS micromachining technology. The deep reactive ion etching (DRIE) technology is used to pattern the HSA from silicon-on-insulator (SOI) wafer. The hydrofluoric acid solution is used to etch the thermal oxide layer beneath H-shape of silicon on insulator wafer in wet etching. But the thermal oxide layer remains there as it without under the four anchors of the HSA. The metal inter-connect to the dielectric inter-layer and CMOS foundry silicon substrate in post-CMOS micromachining technology. The compatible voltage and current with standard IC (CMOS) are applied to operate the actuator by the polysilicon resistivity. We apply the DC voltage to the both anchors of the ZSA beam, current pass through the long beams. High temperature produces due to high current density in long beams according to joule heating effect principle. Therefore some extension produce in the long beams of the actuator due to the thermal expansion in the material and move the beams towards right direction. This direction of motion and the net displacement depends on the applied voltages. The

link beam of the ZSA move towards right direction, as long beam move toward right after thermal expansion. The direction of motion is denoted as x-axis as shown in fig.2.4.

We can obtain the larger displacement by this type of actuator. The anchors and beams of the ZSA have high aspect ratio [19]. Therefore it provide exceptional mechanical stability in the contradiction of mechanical vibrations. As the voltage increases, the output displacement also increases along with large temperature. ZSA is rarely used due to requirement of comparatively high operating voltages (typically up to 22V) but it is used in many industrial applications like variable optical attenuators (VOA). A comparison chart of USA, VSA, ZSA and HAS is given in table 2.1

Table 2.1 Comparison among different MEMS ET Actuators

Features	U-Shaped ET Actuator (USA)	V-Shaped ET Actuator (VSA)	Z-Shaped ET Actuator (ZSA)	H-Shaped ET Actuator (HSA)
Beams/Arms	Two hot and cold arms connected to one common fixed end to make U shape	Two hot arms either directly connected or connected to shuttle and make V shape	Two Z-shape hot arms either directly connected or connected to shuttle.	Two hot arms are joint via one link beam in the middle of two hot arms to make H shape
No. of Anchors	2	2	2	4
Displacement	Small	Large	Largest	Intermediate
Voltages	Low	Very Low	Lowest	Intermediate
Switching Speed	Very Slow	Faster than USA	Faster than VSA	Fastest
Power Consumption	High	Lower than USA	Lower than VSA	Highest
Output Force	Not so High	High	Very High	Highest

Chapter 3

Characterization Methodology

3.1 CMOS-MEMS Comb Drive Electro-Thermal (ET) Actuator:

The comb drive CMOS-MEMS resonator device is used for electro-thermal (ET) actuation mechanism in this research work. Briefly describe that comb drive resonator device is actuated electro-thermally using comb fingers inter-digitated with stator comb finger to produce differential amplitude in lateral y direction due to lower stiffness rather than z direction which has more stiffness. The proposed device is a new type of Electro-Thermal (ET) actuator which easy to design, fabricate and implement in the applications which are described in chapter 1. In the past, some thermal actuators are designed for micro grippers, micro mirrors, micro pumps and biomedical applications, although that are easy to integrate with electronics and low cost for batch fabrication but constrained to poor actuation mechanism with comparatively large driving voltage, power consumption, low amplitudes and force. The Ataman *et al* and Farooq Ahmad *at el* describe the new type of resonant based device which provide the excellent performance to achieve maximum amplitude, force at minimum driving voltages and power consumption [36].

This device consist of central shuttle rotor and stator which is associated with comb fingers and four long beams. The rotor fingers are interdigitated with the stator finger. The four polysilicon PZR are also attached at the four long beams of the device. These polysilicon PZRs are used as active resistors embedded on the long beams near by the anchors [37].

The device was fabricated using three metal and two poly silicon material by 0.35 μ m CMOS MEMS technology. The comb finger resonator device was released by dry post micromachining technology using DRIE machine (Tegal SS110A) at Bhd. The detail description is given in [38]. The fabrication of this shuttle based CMOS-MEMS resonator device was finalized at MIMOS Bhd Company in Malaysia. The wafer was thinning from back side by grander machine (DISCO DFG 840) from

700 μm to 400 μm in first step. Silicon (Si) was etched selectively from back side of wafer about 360 μm depth in second step. During the etching of Si and SiO₂ from front side of the wafer, top metal (metal 3) used as mask layer in third step and finally the device structure is fully released. The material properties which are used to release this comb finger thermal actuator device is given below in table 3.1.

Table 3.1 Material Properties of CMOS-MEMS ET Actuator

Sr.#	Material	Symbol	Young's Modulus (GPa)	Density (Kg/m ³)
1	Silicon dioxide	SiO ₂	73	2648
2	Silicon	Si	130	2328
3	Aluminum	Al	77	2700
4	Polysilicon	Si _{poly}	169	2300

3.1.1 Design Parameters of CMOS-MEMS Device:

The top view of CMOS-MEMS device consists of central shuttle and four supported long beams (two beams left and two beams right side of central shuttle) are shown in fig. 3.1. The fingers of upper side of the central shuttle (rotor part) are overlapping side by side along with the fingers of top surface (stator part) and the fingers of lower side of the central shuttle (rotor part) are overlapping side by side along with the fingers of bottom surface (stator part). Notice that the fingers of central shuttle which are just overlapping side by side with the fingers of stator part of the resonator (upper and lower surface) having dimensions 385 μm ×200 μm . these fingers are not touching to the overlapping fingers because there is gap between the overlapping fingers is 3 μm . Length of each finger is 60 μm but the overlapping length of both sided fingers are 30 μm . Spacing between the central shuttle fingers (rotor part), top and bottom surface fingers (stator part) are 9 μm while width of each finger is 3 μm . The device structure is given below in fig. 3.1

The central shuttle has dimension 155 μm ×100 μm length and width respectively while outer length of the shuttle is 310 μm where the figures of the rotor part are connected at both top and bottom side of central shuttle. Four long beams (two left side and two right side) whose length is not designed more than 300 μm , while the gap between the two beams are 33 μm which are attached to left or right side of the shuttle as shown in fig. 3.1[39] . So these long beams are used to connect with

anchors for biasing purposes. The design parameters of comb drive CMOS-MEMS resonator device which is used for ET actuation mechanism are given in table 3.2.

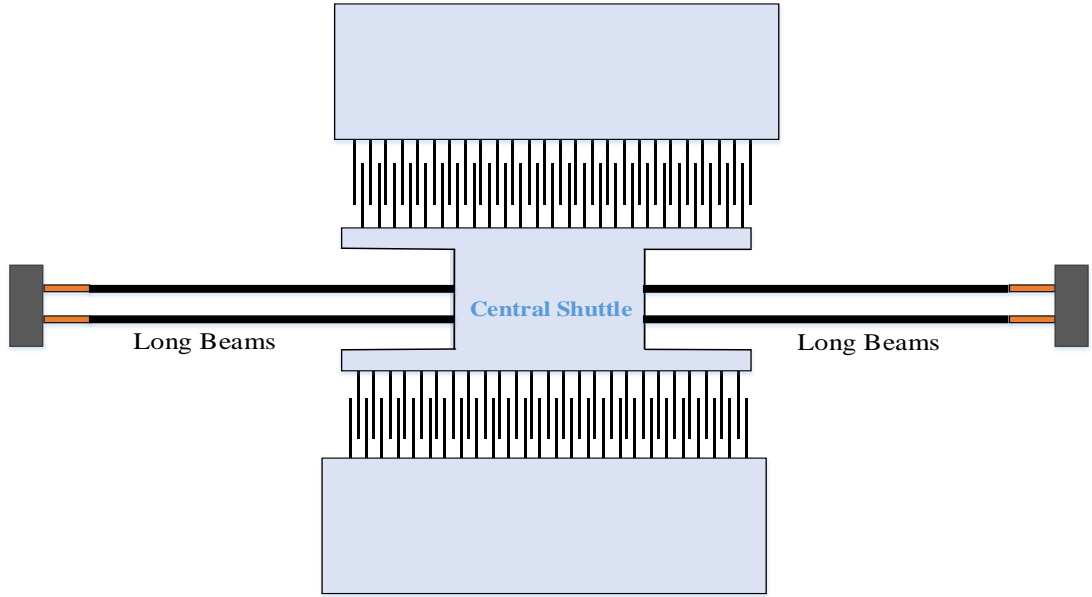


Figure 3.1 Central Shuttle based Comb Drive Electro-Thermal (ET) Actuator [39]

Table 3.2 Design Parameters of Resonating Comb Drive ET Actuator

Sr.#	Symbols	Parameters	Value (μm)
01	l_d	Device length	755
02	w_d	Device width	680
03	l_b	Long beam length	300
04	w_b	Long beam width	3
05	t_b	Long beam thickness	5
06	l_{shuttle}	Shuttle length	155
07	w_{shuttle}	Shuttle width	100
08	t_{shuttle}	Shuttle thickness	5
09	l_{finger}	Shuttle finger length	60
10	w_{finger}	Shuttle finger width	3
11	t_{finger}	Shuttle finger thickness	5
12	$l_{\text{stator.fing}}$	Stator finger length	60
13	$w_{\text{stator.fing}}$	Stator finger width	3
14	$t_{\text{stator.fing}}$	Stator finger thickness	5
15	$A_{\text{etch.hole}}$	Etch hole size	10×10
16	m_{shuttle}	Mass of the shuttle	541.29×10^{-12}

3.2 Device Actuation Principle:

When the AC current applied to the anchors of long beams and passes through the long beam and central shuttle as well, the temperature of long beams and central shuttle of MEMS resonator device increases and becomes heated up according to material thermal expansion coefficient (TEC). So the electrical energy is converted

into the thermal energy. This conversion of energy is called joule heating effect. Thermal expansion can be produced in the long beams of the device in the consequence of joule heating effect according to its working principle. The thermal expansion causes to resonate the shuttle in y direction as shown in fig.3.2. The temperature coefficient of resistance (TCR) of the material changes as the temperature of central shuttle and long beams changes. The impact of joule heating on the shuttle based electro-thermally actuating device which was fabricated using 0.35μm CMOS-MEMS technology can be determined. The Eq.3.1 is given for raise of temperature in resonating shuttle which is independent time [38].

$$t_{\max(x=l/2)} = t_{amb} + \frac{1}{2k_e} \frac{v_a^2 A_{m2} (l/2)^2}{\rho_e l V} \quad (3.1)$$

Where t_{amb} is the ambient temperature, v_a is the resonating central shuttle actuation voltages, A_{m2} is the area of cross sectional of metal 2, l is the resonating central shuttle length, k_e is the effective thermal conductivity, ρ_e is the electrical resistivity, V is the central shuttle volume and t_{\max} is the maximum temperature of central shuttle.

3.3 Biasing of CMOS-MEMS ET Actuator:

The central shuttle is the core part of the device which resonates at applied AC current. It is connected to the different part of the device electrically and mechanically. The four long beams are the one sided fixed which are directly connected to the resonating central shuttle of the device which is rotor as shown in fig 3.2 (a). These long beams are used to connect anchors to the device. Other thing is important to note that both sides of stator (top and bottom side) parts are grounded. Therefore, there will be no capacitive effect in the interdigitated fingers of the resonating rotor part and stator part of the device.

This device is either actuated at constant AC current or at driving frequency or at any desire frequency. When the alternating current (AC) is applied to anchors suspended to the long beams, passed through the long beams in x direction. The current i is equally divided to two parts i_{x1} and i_{x2} in upper and lower long beam as shown in fig.3.2 (a). The current i_{x1} enters in metal 2 (yellow color metal) and further spreads into three metal parts followed by metal 1 (green color metal), metal 2 (yellow color metal) and metal 3 (orange color metal) which are denoted by i_{x1M1} , i_{x1M2} and i_{x1M3} respectively for upper long beam as shown in fig. 3.2 (b). Similarly, the

current i_{x2} also enters in metal 2 (yellow color metal) and further spreads into three metal parts followed by metal 1 (green color metal), metal 2 (yellow color metal) and metal 3 (orange color metal) which are denoted by i_{x2M1} , i_{x2M2} and i_{x2M3} respectively for lower long beam as shown in fig. 3.2 (b) . These three metals are connected each other through vias filled by the tungsten plugs which are explained by the cross sectional view of the beams and fingers of central shuttle in fig. 3.2(c) [38].

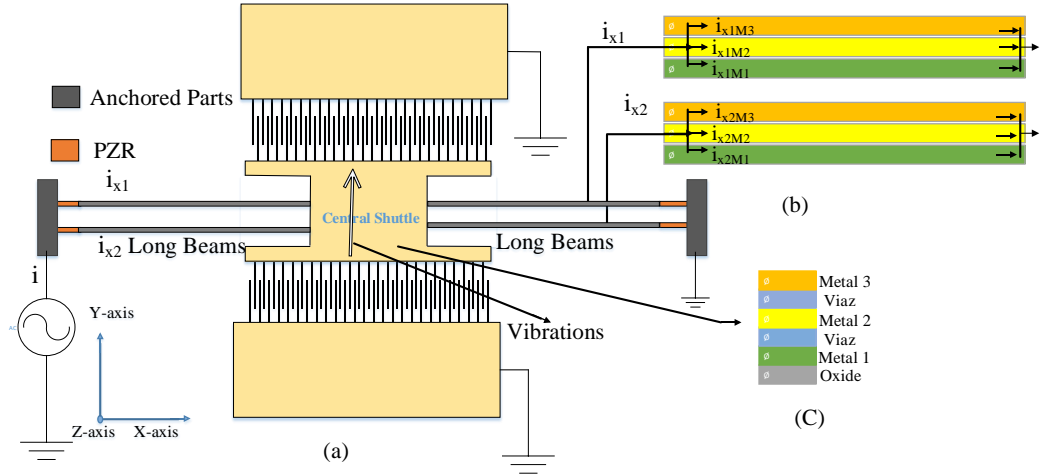


Figure 3.2 (a) Resonating Comb Drive Electro-Thermal (ET) Actuator, (b) Cross Sectional View of Long Beams, (c) Cross Sectional Layers Scheme of Central Shuttle [38]

$$i = i_{x1} + i_{x2} \quad (3.2)$$

$$i_{x1} = i_{x2} \quad (3.3)$$

$$i_{x1} = i_{x1M1} + i_{x1M2} + i_{x1M3} \quad (3.4)$$

$$i_{x2} = i_{x2M1} + i_{x2M2} + i_{x2M3} \quad (3.5)$$

The long beams are designed in such a way that there are two different materials having different temperature coefficient of resistance (TCR) and different thermal expansion coefficients (TEC) are used such as three aluminum layers with alternatively silicon dioxide (SiO_2) layers. The two polysilicon layers are also deposited with alternative silicon dioxide (SiO_2) layers between three aluminum metal layers and silicon substrate. These long beams have lower stiffness in y direction as compared to z direction. When alternating current (AC) is applied through the anchors part and pass through these long beams. The material having higher TEC expands more rapid than the lower TEC according to the joule heating effect. The expansion of the long beams is denoted by ∇l . Therefore, the long beams moves upwards (y-axis) due to having higher TEC material at the upper layers of the beams. This displacement leads to move the central shuttle upward. The shuttle displacement (d_l) is produced due to long beams elongation is calculated theoretically by Eq. 3.6 [40].

$$d_l = [l^2 + 2(l)\nabla l - l \cos(\alpha)^2]^{\frac{1}{2}} - l \sin(\alpha) \quad (3.6)$$

Where l is the length of long beams of resonating central shuttle, ∇l is the elongation of the length of long beams and α is the angle between the deflection position of the long beams and initial position of the long beams. The shuttle displacement (d_l) is multiplied by the stiffness of the central shuttle, the output thermal force (F_T) is determined. The thermal force (F_T) is produced in the long beams which is applied to the shuttle by the long beams can be calculated by Eq. 3.7 [41].

$$F_T = \frac{Etw^3d_l}{4l^3} \quad (3.7)$$

Where E young's modulus, d_l is the displacement produced in long beams, l, w and t is the length, width and thickness of the long beams which are supporting to resonating central shuttle. When AC current is applied, the differential amplitude (∇A) is produced in the consequence of displacement (d_l) produced in the central shuttle. The maximum differential amplitude is also obtained when the driving frequency become equal to central shuttle natural frequency. The detail description of differential amplitude (∇A) and maximum differential amplitude (∇A_{max}) is given in 3.4.1 and 3.4.2.

3.4 Mechanical Modelling of Device:

The mechanical behavior of the oscillating beams of CMOS-MEMS ET actuator thermal force (F_T) is given the following spring- mass system non-homogeneous 2nd order differential Eq.3.8 [42]:

$$m\ddot{Y} + b\dot{Y} + kY = F_T \cos \omega_d t \quad (3.8)$$

Where m, b, k and F_T are the device effective mass, damping factor, effective spring constant and the thermal force of the resonator device resonating in y direction. Y is the resonator displacement in y direction. It is the continues system with driving frequency ω_d having amplitude of thermal force (F_T) which act as driving force for the central shuttle to oscillate in y direction. The Eq.3.8 is the real part of the following complex form of simplest 2nd order differential Eq.3.9:

$$\ddot{Z} + \gamma\dot{Z} + \omega^2 Z = \frac{F_o}{m} e^{j\omega_d t} \quad (3.9)$$

The complete solution (general solution) of real non-homogeneous 2nd order differential equation consist of sum of complementary solution and particular

solution. The complementary solution is also known as transient solution while the particular solution of non-homogeneous 2nd order differential equation is known as steady state solution. Transient solution depends upon the initial condition of the system while the steady state solution depends on the driving frequency (ω_d), driving amplitude force (F_T), natural frequency (ω_o) and damping ratio of the system. As we are interested to determine the differential amplitude (∇A) of the shuttle based resonating thermal actuator, the system is kept under continuous resonance during its operation. Therefore, we limits the solution of above system to obtain only steady state solution of non-homogeneous 2nd order differential equation. The steady state solution of non-homogeneous 2nd order differential equation can be determined by Eq.3.10:

$$Y_{SS}(t) = A \cos \omega_d t + B \sin \omega_d t \quad (3.10)$$

By taking the 1st and 2nd derivative (see Appendix I) of Eq.3.10, substituting the values of $\ddot{Y}_{SS}(t)$, $\dot{Y}_{SS}(t)$, and $Y_{SS}(t)$ in Eq.3.8 and rearranging the terms, we get

$$(-\omega_d^2 m A + \omega_d b B + k A) \cos \omega_d t + (-\omega_d^2 m B - \omega_d b A + k B) \sin \omega_d t = F_T \cos \omega_d t \quad (3.11)$$

By Comparing coefficient of $\cos \omega_d t$ and $\sin \omega_d t$, we get system two linear equations (see Appendix I). By solving this system of equation to get values of A and B (see Appendix I), which is substituted in Eq.3.10, we get the steady state solution of non-homogeneous 2nd order differential equation is obtained by Eq.3.12:

$$Y_{SS} = \left\{ \frac{\frac{F_T}{m} (\omega_o^2 - \omega_d^2)}{(\omega_o^2 - \omega_d^2)^2 + (\gamma \omega_d)^2} \right\} \cos \omega_d t + \left\{ \frac{\frac{F_T}{m} (\gamma \omega_d)}{(\omega_o^2 - \omega_d^2)^2 + (\gamma \omega_d)^2} \right\} \sin \omega_d t \quad (3.12)$$

3.4.1 Output Differential Amplitude:

When AC applied to the comb drive ET actuator, the rotor part resonate in lateral direction (along y axis) rather than z-axis in the consequence of long beams deflection or displacement (d_l) along y-axis. When the electric AC current pass through central shuttle via long beams, the electrical energy is converted into thermal energy and the central shuttle heated up. The central shuttle starts resonating in y direction in form of vibration at its applied AC current with some driving frequency. A differential amplitude is obtained which is denoted by ∇A . The output differential amplitude of the resonant shuttle is determined by using optical method

experimentally. It can also be determined using steady state solution of the above non-homogeneous 2nd order differential equation theoretically. We determined the output differential amplitude of central shuttle based resonant device under the ET actuation by the equations detail in Appendix I. Thus the output differential amplitude (∇A) is calculated by Eq.3.13 as [43]:

$$\nabla A = \frac{\left(\frac{Etw^3d_l}{4l^3}\right)/m}{\sqrt{(\omega_o^2 - \omega_d^2)^2 + (\gamma\omega_d)^2}} \quad (3.13)$$

Where m is the effective mass of the resonating device under thermal actuation force, ω_o , ω_d and γ are the natural frequency, driving frequency of the central shuttle and the damping constant. The relation among the damping ratio (ξ) and natural frequency (ω_o) is given by Eq.3.14:

$$\gamma = 2\xi\omega_o = \frac{b}{m} \quad (3.14)$$

3.4.2 Maximum Differential Amplitude:

When the driving frequency (ω_d) is increased in such a way that driving frequency (ω_d) become equal to central natural frequency (ω_o), then the resonance occurs. The frequency at this stage is known as resonance frequency. When driving frequency reaches to the central shuttle mechanical/fundamental frequency at first mode of resonance, maximum differential amplitude (∇A_{max}) is produced. It produces maximum vibration in the resonating central shuttle. This maximum differential amplitude (∇A_{max}) may be sensed by various methods such as piezoelectric, piezoresistive, electromagnetic and optical method. We have determined the maximum differential amplitude (∇A_{max}) by optical sensing method as already described. The maximum differential amplitude (∇A_{max}) can also be calculated theoretically by given Eq. 3.15:

$$\nabla A_{max} = \frac{\left(\frac{Etw^3d_l}{4l^3}\right)}{m\omega_o\gamma} \quad (3.15)$$

3.4.3 Phase shift:

The phase (δ) of the oscillating shuttle based resonant device is also depends upon the driving frequency (ω_d) of the central shuttle. The phase shift can be determined by the Eq. 3.16 and detail is given in appendix I:

$$\delta = \tan^{-1} \left(\frac{\gamma \omega_d}{\omega_o^2 - \omega_d^2} \right) \quad (3.16)$$

The maximum phase shift is $\pi/2$ radians, when the resonance occurs.

3.4.4 Damping Ratio:

The damping ratio of the resonating shuttle based MEMS actuator is defined as the ratio of damping constant to the double of natural frequency of the resonating device. In other words, damping ratio is also defined as the ratio of actual damping coefficient to the critical damping coefficient of the resonating device. Thus theoretically, the damping ratio is calculated by the Eq.3.17:

$$\xi = \frac{\gamma}{2\omega_o} = \frac{1}{2Q} = \frac{b}{2m\omega_o} = \frac{b}{b_c} \quad \text{Where } b_c = 2\sqrt{km} \quad (3.17)$$

Where Q is the quality factor b is the actual damping and b_c is the critical damping.

3.4.5 Quality Factor:

The quality factor (Q) is one of the important parameter which tell about the performance of the resonating actuator device. It can be determined from the behavior of the resonance. Further, the ratio of the energy stored to the energy loss per cycle in the system is also called quality factor (Q). Actually, the quality factor of the device describes response of the resonating MEMS device at specific frequencies. Mathematically, the quality factor of the electro thermally actuated MEMS resonator is determined by the Eq. 3.18 [44]:

$$Q = \frac{\omega_o}{\gamma} = \frac{f_r}{\Delta f_{3dB}} = \frac{m\omega_o}{b} = \frac{1}{2\xi} \quad (3.18)$$

Where Δf_{3dB} is the difference between two frequencies f_1 and f_2 at half power beamwidth and f_r is the resonance frequency.

3.4.6 Device Damping:

There are many mechanisms of damping in the central shuttle based CMOS-MEMS resonant device which loss the energy. The friction between the gaseous environment and micro machine resonant ET actuator device is one the important damping mechanism [42]. There are various components of air damping force for shuttle based comb resonator according to the different damping mechanisms. The main components of damping friction are given as follows.

3.4.6.1 Slide-film Bottom Damping Force:

The gap distance d_p between the substrate and resonating central shutting is much smaller than effective delay distance (δ). The some sort of coquette-flow type damping force is given in Eq. 3.19:

$$F_1 = \mu \frac{A_p}{d_p} \dot{x} = C_1 \dot{x} \quad (3.19)$$

Where A_p is the effective area of the whole resonating device including area of long beams, central shuttle which is resonating and even hole etch area. Although the dimensions of the hole etch area is even small that the air flow in the hole laterally does not exist. The viscosity of the air is denoted by μ . It is the most important damping frictional force component from out of all components.

3.4.6.2 Slide-film Top Damping Force:

Consider the case that the resonating device structure is at some distance from the objects which are above on it. The some sort of stokes-flow type damping frictional force above the moving part of the resonating shuttle based device is appeared. Thus the damping frictional force is given in Eq.3.20:

$$F_2 = \mu \frac{A_p}{\delta} \dot{x} = C_2 \dot{x} \quad \text{Where } \delta = \sqrt{2\mu/\rho_{air}w} \quad (3.20)$$

Where the air density is denoted by ρ_{air} while the δ is the effective delay distance.

3.4.6.3 Slide-film Sidewalls damping force:

The sidewalls damping frictional force is given by Eq.3.21:

$$F_3 = \mu \frac{A_p}{d_s} \dot{x} = C_3 \dot{x} \quad (3.21)$$

Where the d_s and A_p are the gap distance between the fixed fingers and the sidewalls and moving fingers sidewalls area respectively. But we consider here that gap distance (d_s) is much smaller than the effective delay distance (δ).

The total damping frictional force F on resonating shuttle is the sum of above three components of damping forces as follows:

$$F = \mu \frac{A_p}{d_p} \dot{x} + \mu \frac{A_p}{\delta} \dot{x} + \mu \frac{A_p}{d_s} \dot{x} \quad (3.22)$$

$$F = (C_1 + C_2 + C_3)\dot{x} \quad (3.23)$$

3.4.7 Spring Constant:

One of the important parameter is the spring constant. The spring constant tells the characteristics of resonating thermal actuator. We analyze the behavior of the flexural long beams of the resonating device by the calculation of spring constant mechanically. The static bending of the long beams can be calculated by Eq.3.24 [45]:

$$k_b = \frac{F}{Y_{dis}} = \frac{12EI}{l^3} = \frac{Et w^3}{l^3} \quad \text{Where} \quad I = \frac{1}{12} t w^3 \quad (3.24)$$

Where I is the moment of inertia l is the length, w is the width and t is the thickness of the long beam while k_b is the individual beam spring constant.

$$k_y = N k_b = N \frac{Et w^3}{l^3} \quad (3.25)$$

Where E is the young's modulus of elasticity, N denotes the total numbers of long beams attached to the resonating shuttle and K_y denotes the overall spring constant of the whole resonating actuator in y direction.

3.4.8 Resonance Frequency (f_r):

Resonance frequency (f_r) of this resonating device is determined experimentally using optical method in this research work. The theoretical calculation can also be measured. So, the Rayleigh method is one of key method to determine the resonance frequency of the resonating device. This is based on varying mass and stiffness distribution. Therefore, this easy to use in this type of resonating MEMS devices. The resonance frequency can be derived by the Eq.3.26 [45]:

$$f_r = \frac{1}{2\pi} \sqrt{\frac{4 \left(\frac{Etw^3}{l^3} \right)}{\rho_{av}(V_s + V_b)}} \quad (3.26)$$

Where K is the overall spring constant of the whole resonating actuator with total four number of beams in y direction, m is the effective mass of whole resonating actuator which is $m = \rho lwt = \rho V = \rho_{av}(V_s + V_b)$. V_s denotes the volume of the central shuttle and V_b denoted the volume of four long beams attached to the central shuttle while ρ_{av} is the average density which is defined by the Eq.3.27:

$$\rho_{av} = \frac{\rho_{SiO_2} \times t_{SiO_2} + \rho_{Al} \times t_{Al}}{t_{SiO_2} \times t_{Al}} \quad (3.27)$$

3.5 Temperature of Device:

The six polysilicon piezoresistor (PZR) are suspended to the long beams of the resonating central shuttle device. The four polysilicon PZR are used as active resistors which are attached at the four long beams edges near by the anchors while two PZR are used as passive resistors in the lower stator part of stator. When the AC current pass through the long beams as well as the central shuttle, the temperature is produced due to the joule heating effect as describes above. The central shuttle starts oscillation and the stress is applies on the PZR suspended of long beam. The temperature rises on the PZR in the consequence of stress applied. This raise in temperature is sensed through the PZR. The value of the PZR changes linearly as the temperature of the resonating device changes. This effect completely described in next chapter. But the temperature sensor (PZR) electrical resistance can be calculated by the Eq.3.28 [46]:

$$R = \rho \frac{l}{A} \quad (3.28)$$

Where l, A and ρ are the length, cross sectional area and resistivity of the aluminum material. The value of resistivity of aluminum material is $2.82 \times 10^{-8} \Omega m$. The relationship between the resistance and the temperature is given in form of resistance as a function of temperature (at low temperature from 0 to 600°C) which can be expressed by Eq. 3.29:

$$R(t) = R_o \{1 + \alpha(t - t_o)\} \quad (3.29)$$

Where α temperature coefficient of resistance (TCR), R is the resistance of the temperature sensor (PZR) at t temperature and R_o is the resistance at ambient temperature t_o .

3.6 Experimental Setup:

The characterization is an important step to study the characteristics of MEMS devices after its fabrication and testing. The resonant central shuttle based comb drive CMOS-MEMS ET actuator has been already fabricated. The characterization of this device has been performed to investigate the various characteristics of the device such as differential amplitude, maximum differential amplitude, driving voltages, resonance frequency, damping constant, damping coefficient, damping ratio, quality factor, output force and sensitivity etc. There are various methods to characterize the resonant comb drive CMOS-MEMS ET actuator. There, we have chosen following experimental setup with optical characterization method. The Optical characterization experimental setup is used to avoid the interfacing of the electromagnetic signals [43]. The experimental setup of this research work comprises following three steps.

1. Surface Analysis using Scanning Electron Microscopy (SEM)
2. Amplitude, resonance frequency and quality factor measurements using Optical Characterization Experimental setup.
3. Output Force Characterization

3.6.1 Field Emission Scanning Electron Microscopy (SEM):

The Field Emission Scanning electron microscopy (SEM) is used to study the detail surface analysis of the MEMS ET actuator. The SEM is the late development due to the involvement of electronics in it. These electronic signals are used to form the 3-dimentional image of the MEMS device by collecting, processing and translating these signals as the pixels on the LCD monitor. These signals interaction reveals information about the MEMS device chemical composition, material orientation, crystalline structure and external texture etc. The SEM scanning image of CMOS-MEMS ET actuator is shown in fig. 3.3 [43] while the Multi Project Wafer (MPW) is shown in fig. 3.4. This scanning image of the MEMS ET actuator is displayed to on the LCD monitor which we analyzed. Finally we analyzed the surface of the MEMS ET actuator under different thermal biasing. We analyzed that surface is

clear and no any debris found on the surface of device chip. So it is ready for characterization.

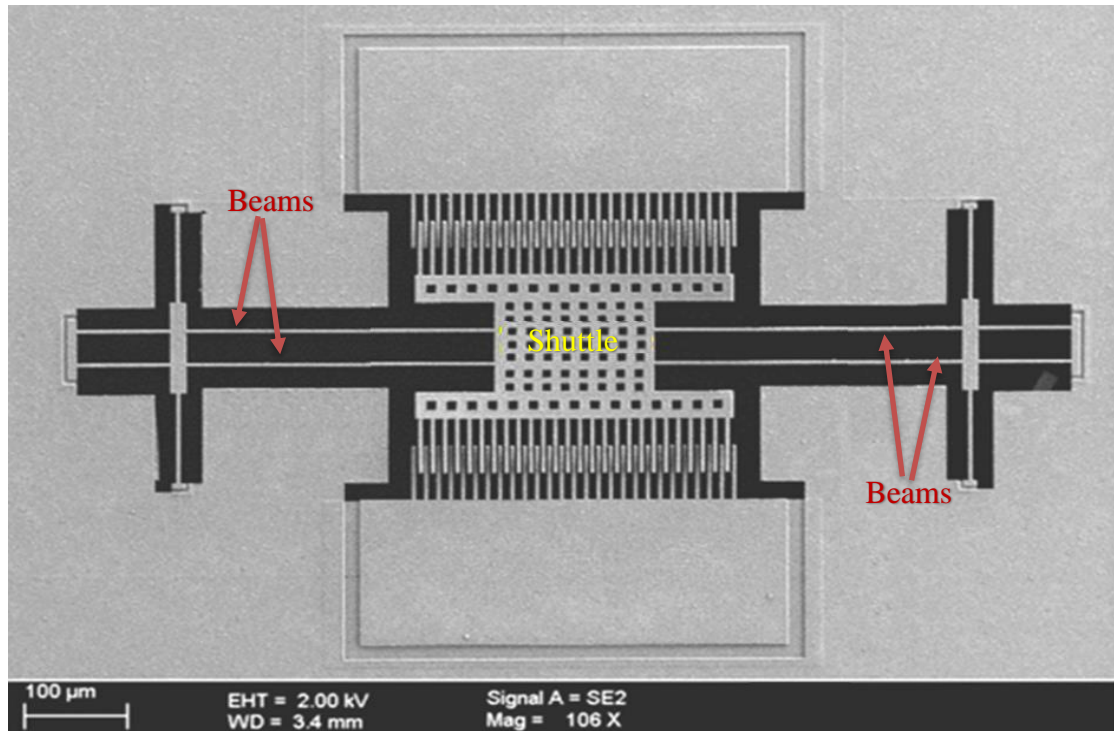


Figure 3.3 FESEM Image of CMOS-MEMS Electro-Thermal (ET) Actuator [43]

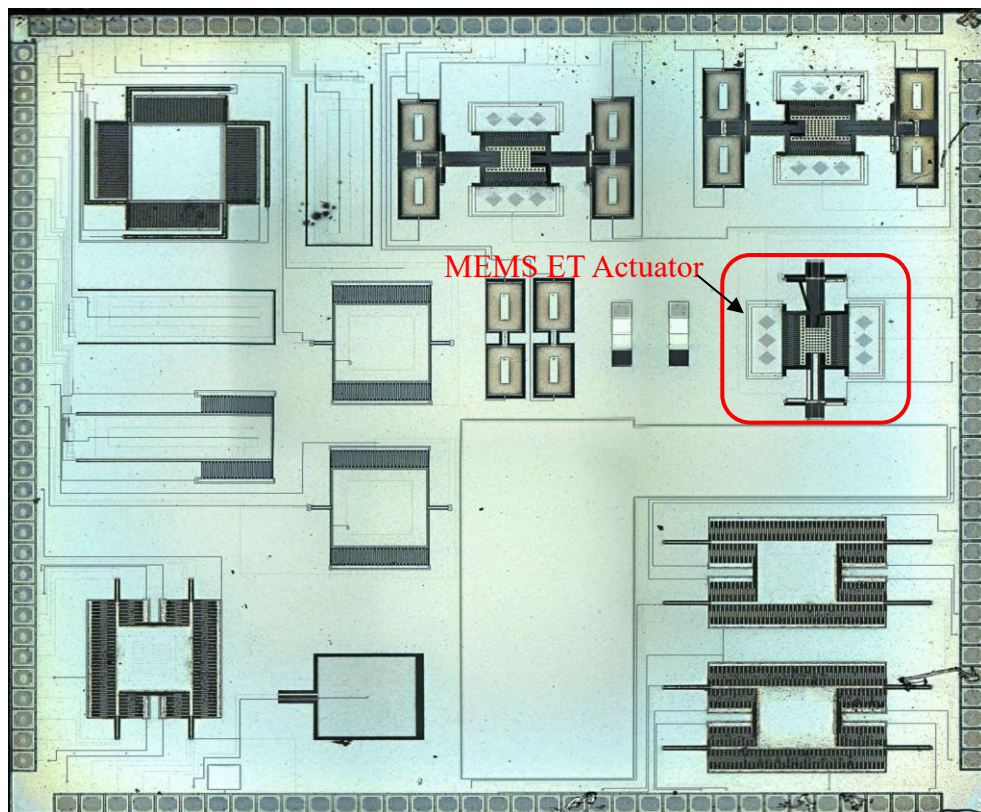


Figure 3.4 Front View of Multi Project Wafer (MPW) Die

3.6.2 Optical Characterization:

The optical characterization of resonating central shuttle based CMOS-MEMS ET actuator encompasses on the standard electrical and optical instruments such as Agilent 33220A function generator, Olympus BX51M optical microscope and LCD monitor. The optical microscope is the core part of this characterization experimental setup. A fine magnification mechanism is used in this technique. The magnified image though Olympus BX51M optical microscope is obtained either on the LCD monitor or captured through the attached CCD camera. The analysis is done by the reference surface and secondary moveable surface. This optical method deals the magnified image of CMOS-MEMS chip by help of stationary reference line surface and moveable secondary surface. The magnified image of the CMOS-MEMS chip is displayed on the LCD monitor. Further photomicrograph image is also captured by the CCD camera attached on the top of the Olympus BX51M optical microscope. This methodology is used to measure the lateral amplitude at resonance frequency of the device. It is good for static, low frequencies (about 10 Hz) and high frequencies (about 10 kHz) as well.

3.6.2.1 Pad connections of the CMOS Chip and DIP:

The apparatuses for the optical characterization experimental setup is organized in such a way that the CMOS-MEMS ET actuator chip is placed under the dual inline package (DIP). The dual inline package (DIP) is jacked into jig. The jig contains 28 female holes (i.e. 14 left side and 14 right side) in which the DIP having 28 legs (14 left legs and 14 right legs) is fixed into the jig.

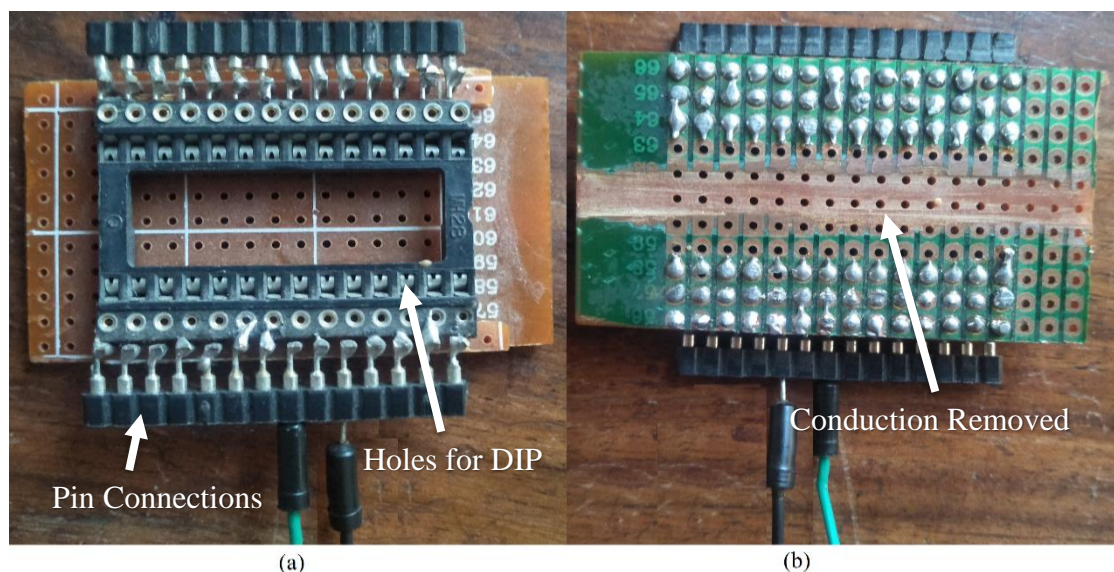


Figure 3.5 (a) Front Side View of JIG (b) Back Side View of JIG

The jig also contains 28 input connection holes (14 left input holes and 14 right input holes) at vertical side. The front side of jig has been shown in fig.3.5 (a), the back side of jig has been shown in fig.3.5 (b). The original chip is placed under DIP which is fixed into jig as shown in fig. 3.6

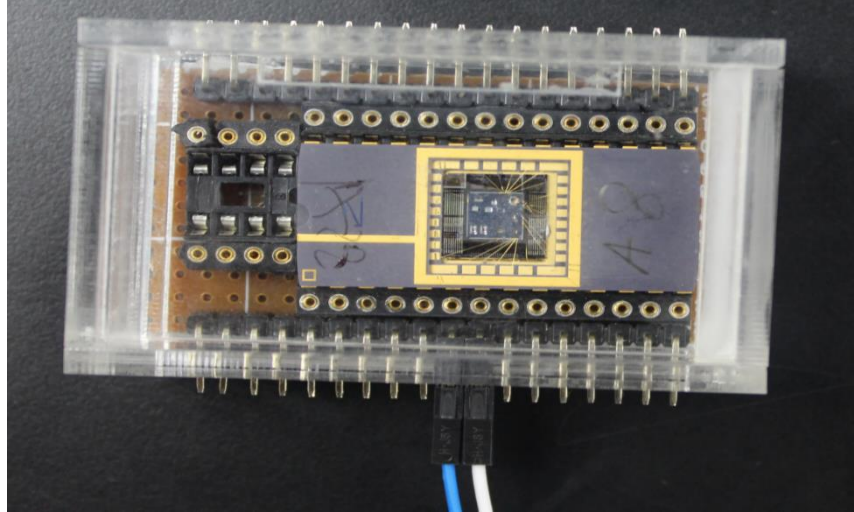


Figure 3.6 The Dual Inline Package (DIP) Placed into JIG

The CMOS-MEMS ET actuator chip under dual inline package (DIP) is shown in fig.3.7.

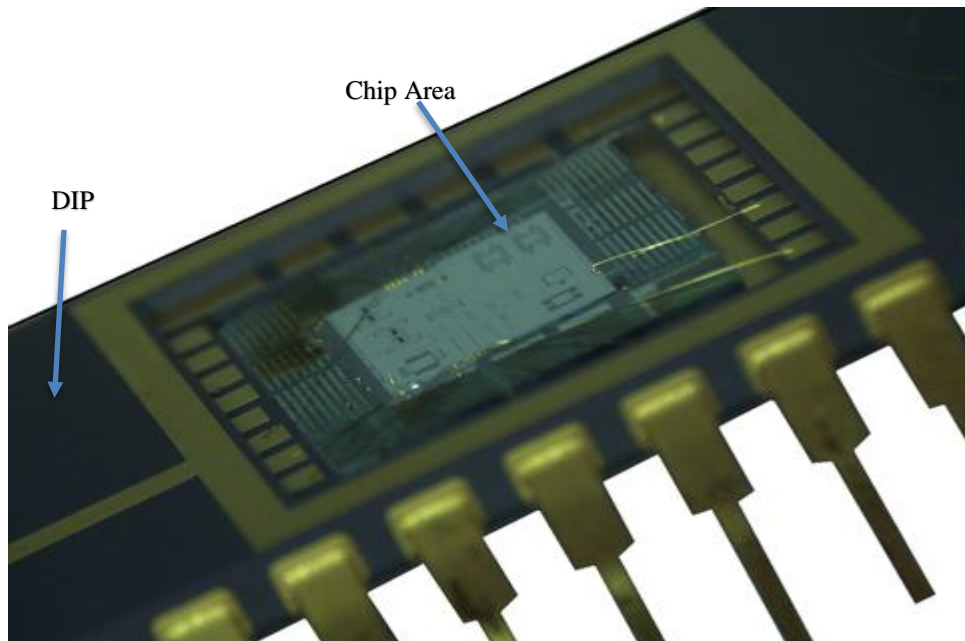


Figure 3.7 The Original CMOS-MEMS ET Actuator Chip Placed Under Dual Inline Package (DIP)

The chip pads configuration with Dual Inline Package (DIP) is given in table 3.3. The gold material is used in the pads of Chip. Therefore, there is golden colors in pads of Chip. The chip is connected to the DIP via Pads in the DIP as well as MEMS chip through gold wiring.

Table 3.3 DIP Vs Chip Pads Connections

Sr.#	DIP Pad No.	Chip Pad No.
01	1	1
02	2	2
03	3	3
04	4	4
05	5	5
06	6	6
07	7	7
08	8	8
09	9	9
10	10	10
11	11	11
12	12	12

Table 3.4 Chip Pad Connections with CMOS-MEMS Device

Sr.#	Pad Description	Pad Symbol	Pad Number
01	Shuttle Biasing	SB	8,10
02	Upper Stator Fingers Biasing	UstatorFB	9
03	Lower Stator Fingers Biasing	Lstator FB	3
04	Longitudinal PZR Left	Long PZR L	4,5
05	Longitudinal PZR Right	Long PZR R	1,2
06	Transvers PZR Left	Trans PZR L	6,7
07	Transvers PZR Right	Trans PZR R	11,12

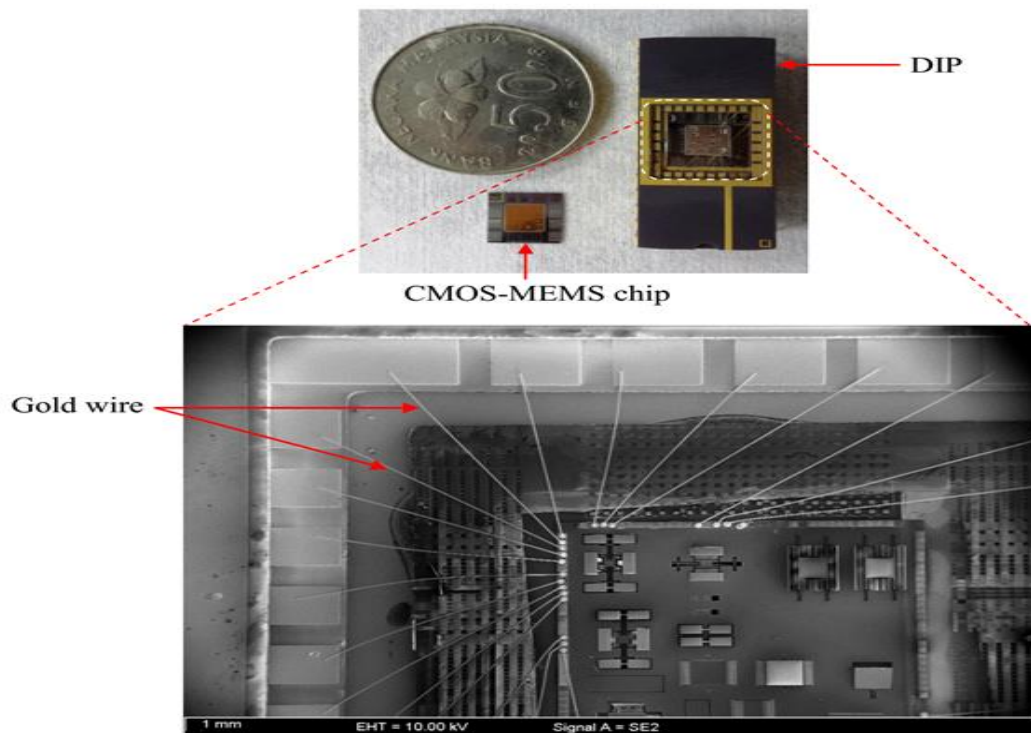


Figure 3.8 Wire Bonding of CMOS-MEMS Chip

The wire bonding is shown in fig. 3.8. The DIP is jacked into the jig in which the input is provided to CMOS-MEMS chips. The whole CMOS-MEMS Chip is Multi Project Wafer (MPW) in which multiple micro devices has been fabricated. But we are characterizing CMOS-MEMS Electro-Thermal (ET) actuator which is enclosed in red color box as shown in fig.3.4. There is necessary to understand the Pad configuration of MPW with CMOS-MEMS ET chip. The Pad configuration of

whole MPW chip with CMOS-MEMS ET chip is given in table 3.4. The Pad configuration with CMOS-MEMS ET actuator chip is shown in fig. 3.9.[45]

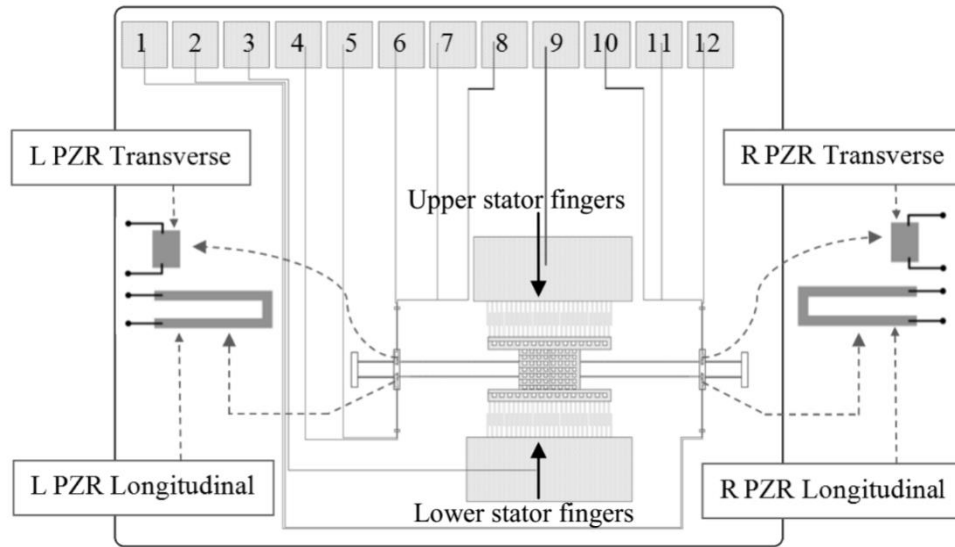


Figure 3.9 The Pad Configuration with CMOS-MEMS ET Actuator Chip [45]

3.6.2.2 Measurement in Static Mode:

The CMOS-MEMS chip under DIP with jig whose amplitude, resonance frequency and quality factor is to be measured is placed under Olympus BX51M Optical Microscope. A DC input current source is connected to the jig via probes to provide the input DC current to anchors of MEMS device. The main heart of this experimental setup is the optical microscope. The magnified image through optical microscope of deflected portion of CMOS-MEMS chip is displayed at LCD.

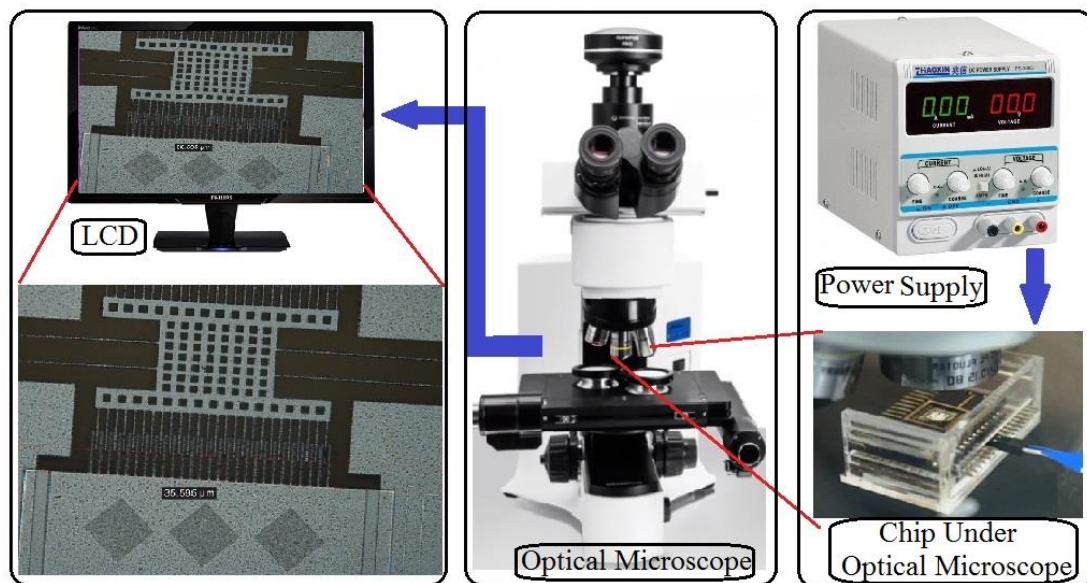


Figure 3.10 Optical Characterization Setup for Static Mode Measurements

A fine image of optical microscope is used to calculate the displacement or sensitivity of the central shuttle fingers via the stationary reference surface and the movable surface in the optical microscope lens. The experimental setup for optical characterization is shown in fig. 3.10. The displacement of the CMOS-MEMS ET chip is displayed with magnification on the LCD screen. Finally the displacement of MEMS device is recorded and observed on screen of LCD.

3.6.2.3 Measurements at Resonance Frequency:

The AC current is applied to the central shuttle CMOS-MEMS ET actuator to study its characteristics at its resonance frequency. The different biasing AC current is applied for its thermal actuation to measure the differential amplitude and sensitivity at its resonance frequency. Initially, AC current 1mA is applied through the signal generator to CMOS-MEMS ET actuator. The differential amplitude is produced in the consequence of central shuttle vibration due to thermal actuation and finally analyzed and recorded. The AC current is gradually increased up to 5mA through the signal generator under driving frequency and the change in differential amplitude and sensitivity due to thermal actuation of MEMS device is analyzed and recorded. The maximum differential amplitude is achieved, when the driving frequency maximizes in such a way that the driving frequency become equal to the resonance frequency. Finally the maximum differential amplitude and sensitivity in terms of differential amplitude are also analyzed and recorded. The experimental setup for optical characterization at resonance frequency is shown in fig. 3.11.

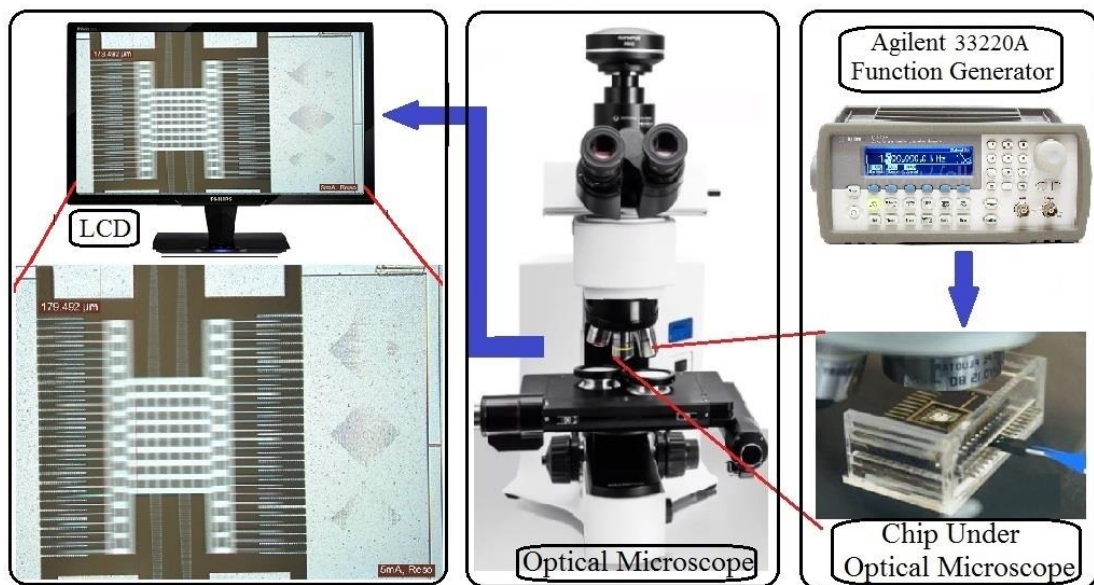


Figure 3.11 Optical Characterization Setup for Resonant Frequency Mode Measurements

3.6.3 Output Force Characterization:

The Output thermal force is approached as the central shuttle displacement found by the experimental calculation. When the input current source is applied to the CMOS-MEMS ET actuator. The displacement is produced in the central shuttle due to the expansion produced and rise in temperature in the long beams of the actuator. This displacement is obtained by optical method as I described in 3.6.2.2. We multiplied the spring constant of CMOS-MEMS ET actuator to this displacement, then obtained the output thermal force.

3.6.4 PZR as Temperature Sensor:

The polysilicon piezoresistors (PZR) are embedded at the end of the four long beams of the CMOS-MEMS ET actuator which is most sensitive part of the actuator. These PZR are used as the temperature sensor in term of change in temperature of the device which effects on the change in resistance. The PZR of the CMOS-MEMS chip is connected ohm meter with the help of connectors and placed the whole device into the chamber to raise the temperature of the device as shown in fig.3.12.

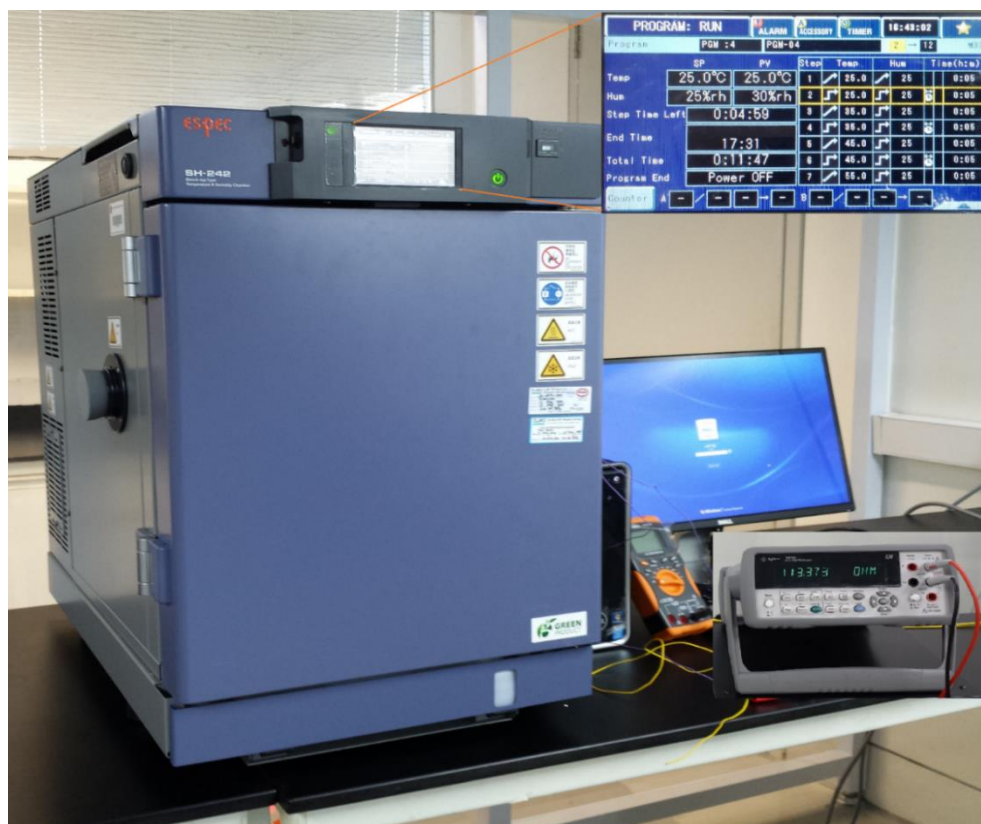


Figure 3.12 Experimental Setup for PZR Resistance Measurement

The UTP has facilitated and helped me to get the experimental reading from its laboratory due to unavailability of this chamber in my institution. Actually, a program is selected for the temperature rise at some specific scale. The temperature rises according to the program selected. So the resistance of the PZR changes as the temperature of the device increases. This change in the resistance is recorded with the help of ohm meter. Therefore, the calibration curve is defined for this in term of change in resistance per degree rise in temperature.

When CMOS-MEMS ET is placed under the optical microscope and provide input current to characterize it, the temperature of the device increase. This increase in temperature is sensed by the change in resistance of the PZR via ohm meter.

Chapter 4

Results and Discussions

4.1 Results:

The results of the ET actuator characterization are obtained theoretically and experimentally. The theoretical analysis is performed by MATLAB and compared to the experimental analysis which is performed by optical characterization method. There are following results which are obtained and compared to the experimental research work.

4.1.1 Input Current Vs Temperature Rise:

Initially, the temperature of the CMOS-MEMS device is assume to be 25°C. The temperature of the device produces as the input current is applies to the device via DC source (static mode). This temperature increases or decreases gradually as the input current increases or decreases according to the joule heating effect principle. The effect of the temperature rise relative to the input current is shown in fig. 4.1.

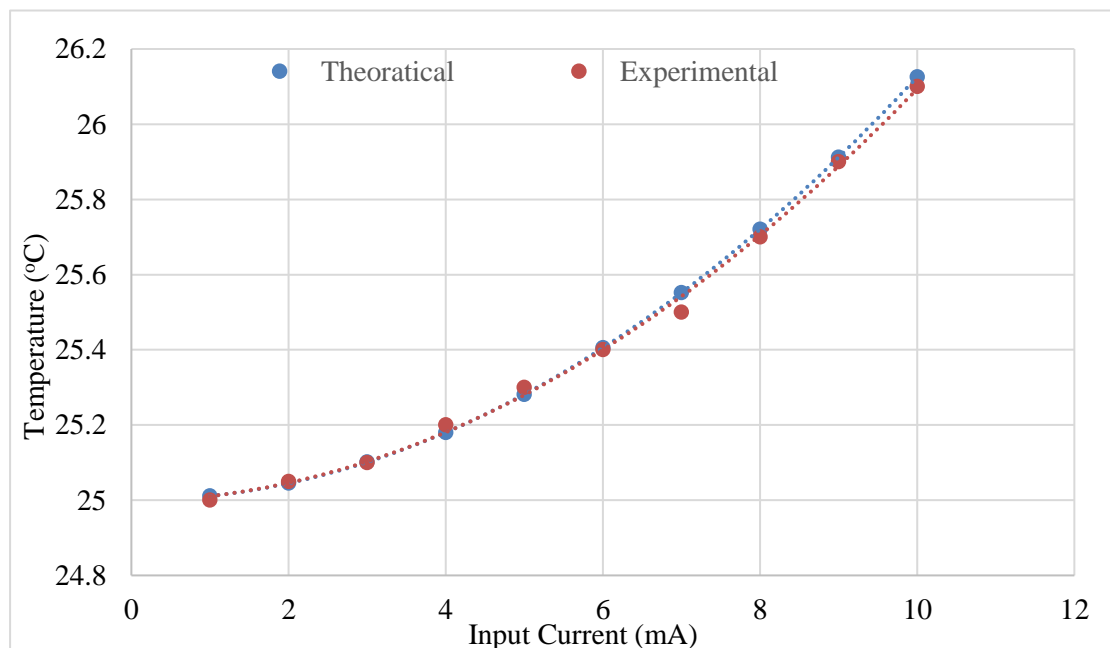


Figure 4.1 Input Current Vs Temperature Change in CMOS-MEMS ET Chip

4.1.2 Input Current Vs Shuttle Displacement:

The shuttle is placed at normal position, when no current is applied. Normally, distance between the central shuttle fingers and stator wall of the device is $30\mu\text{m}$. When the current is applied to the CMOS-MEMS ET actuator which is placed under the optical microscope. The central shuttle is deflected by some micron. This deflection of the central shuttle is recorded on LCD or Laptop screen which is directly connected to optical microscope. As we increase the input current, more deflection of central shuttle is recorded by optical microscope. This change in deflection in the central shuttle from its normal position is called displacement of shuttle. A sample of deflected central shuttle is shown in fig.4.2, when the 10mA input current is applied to the shuttle which produces $5\mu\text{m}$ displacement. There is $35\mu\text{m}$ difference between central shuttle fingers and stator fixed wall is shown in fig.4.2 because the central shuttle is deflected up word by $5\mu\text{m}$. But the normal gap between these two surfaces is $30\mu\text{m}$ as I already described. Thus, the displacement of the central shuttle at 10mA current is $5\mu\text{m}$.

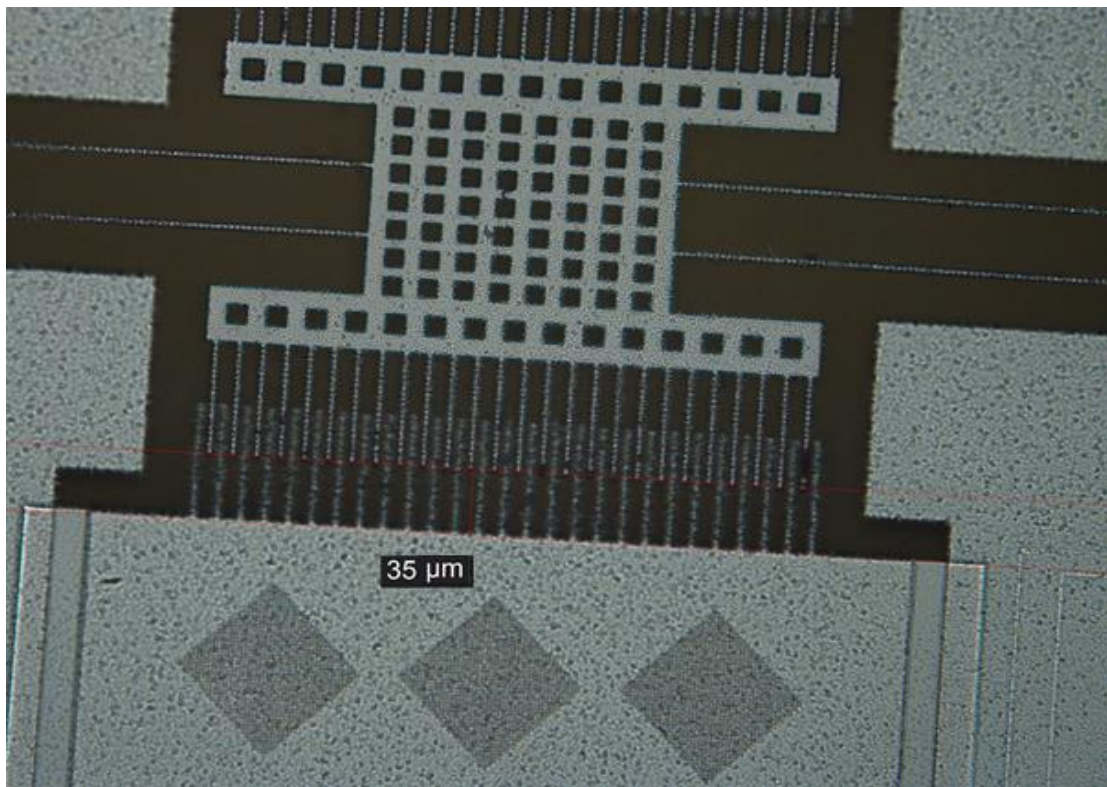


Figure 4.2 Central Shuttle Displacement Measurement in Static Mode

As I already described that the displacement of central shuttle increases or decreases as input current increases or decreases linearly. This linear behavior is shown in fig. 4.3.

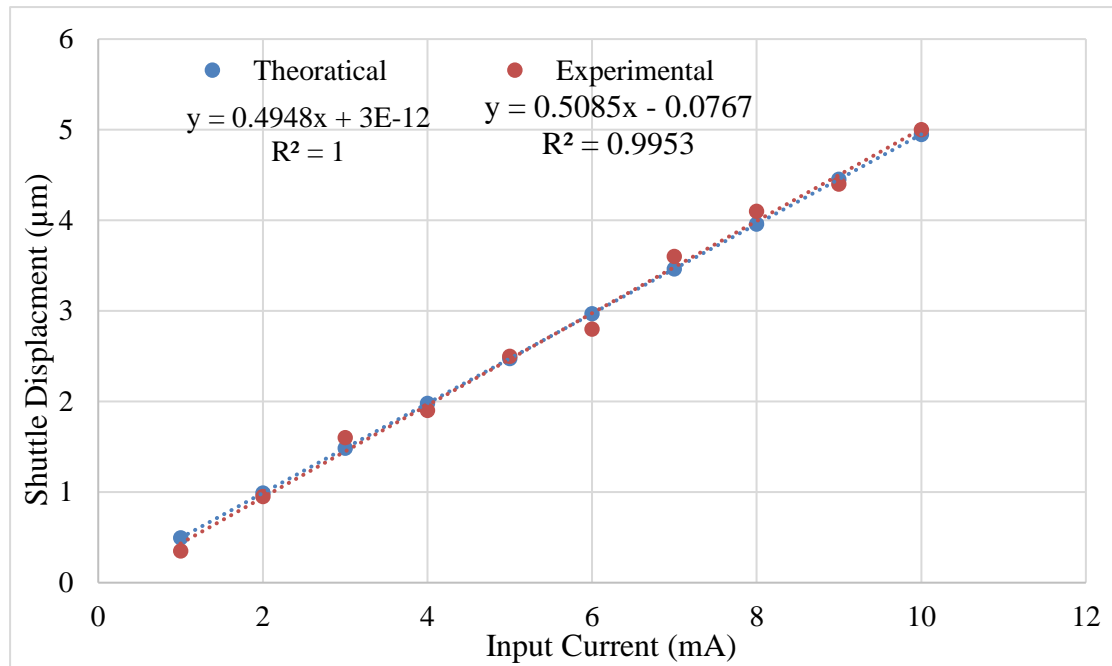


Figure 4.3 Input Current Vs Displacement Produced in Central Shuttle

4.1.3 Input Current Vs Output Thermal Force:

There is no output force when no current passes through the CMOS-MEMS device. As the current pass through the device, displacement produces in the shuttle due to thermal expansion and temperature produced in the four long beams and shuttle. When displacement of the central shuttle is multiplied by the stiffness or spring constant of the CMOS-MEMS device, the thermal output force is obtained. The thermal output force also shows the linear behavior due to linear behavior in displacement of the shuttle as shown in fig.4.4.

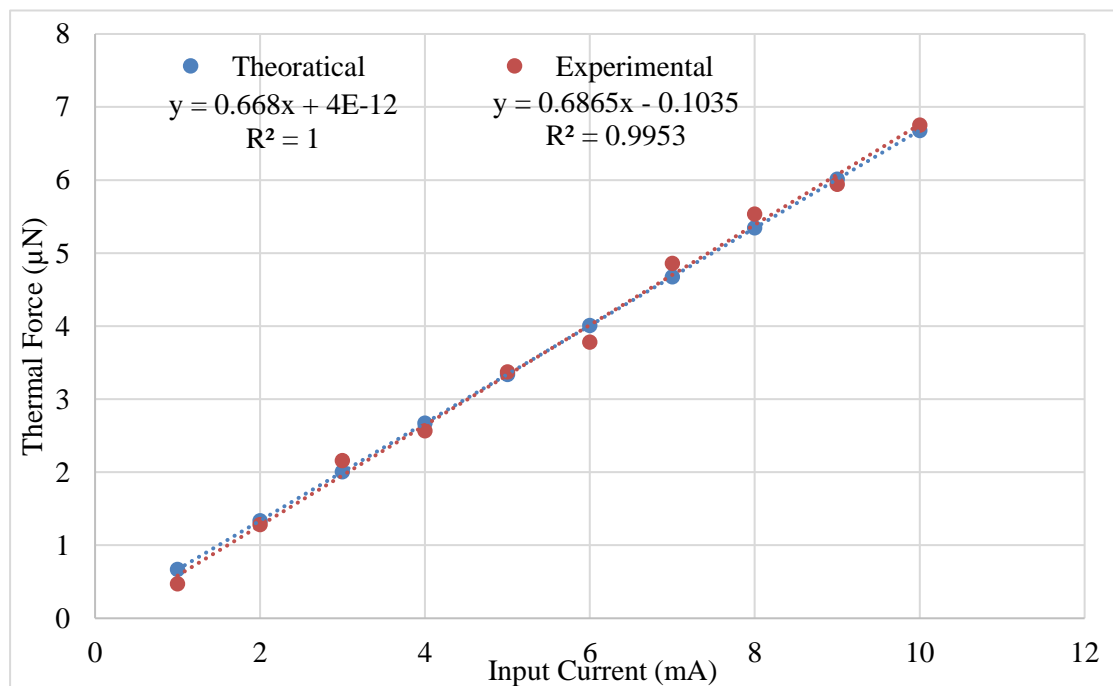


Figure 4.4 Input Current Vs Thermal Force Produced in Central Shuttle

4.1.4 Amplitude Vs Driving Frequency:

When AC input current is applied to the CMOS-MEMS ET actuator which placed under the Olympus BX51M optical microscope. The central shuttle starts vibration in y-axis due to the thermal expansion in the long beams and shuttle displacement produced continuously. When the positive half cycle of the AC current passes through the long beams and central shuttle as well, the central shuttle moves upward (+ve y-axis) while the negative half cycle of the AC current passes through the shuttle causes to compel it downward (-ve y-axis). Therefore, central shuttle vibrates continuously as the AC current passes through the device. The central shuttle reaches its normal position when one cycle of AC current completed or no current passes through the central shuttle.

The maximum amplitude of the central shuttle is obtained at input AC current driving frequency become equal to mechanical resonance frequency. A sample of maximum amplitude at 5mA AC current applied with resonance frequency is shown in fig. 4.5.

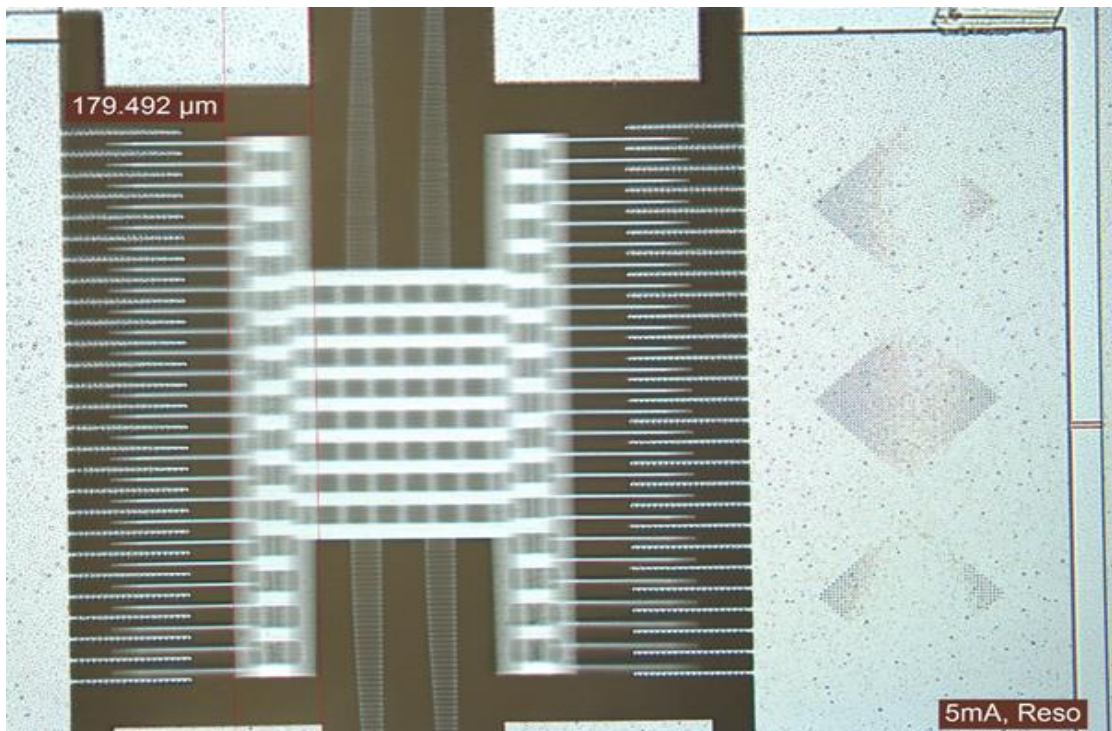


Figure 4.5 Amplitude Measurement at Resonance Frequency

Normally the width of left rod of central shuttle associated with shuttle fingers is 30μm. When the 5mA AC current is passed at its resonance frequency, the central shuttle vibrates at resonance frequency and the width of this rod seems to be

179.492 μm via optical microscope. We subtract the 30 μm from the 179.492 μm and divided by 2 to obtain the one sided maximum amplitude. Therefore maximum amplitude 74.7 μm at 8570Hz resonance frequency is measured by the optical microscope. But the theoretical calculation of the maximum amplitude 72.15 μm at 8596Hz is measured. The obtained the relation of the amplitude vs driving frequency which is shown in fig.4.6.

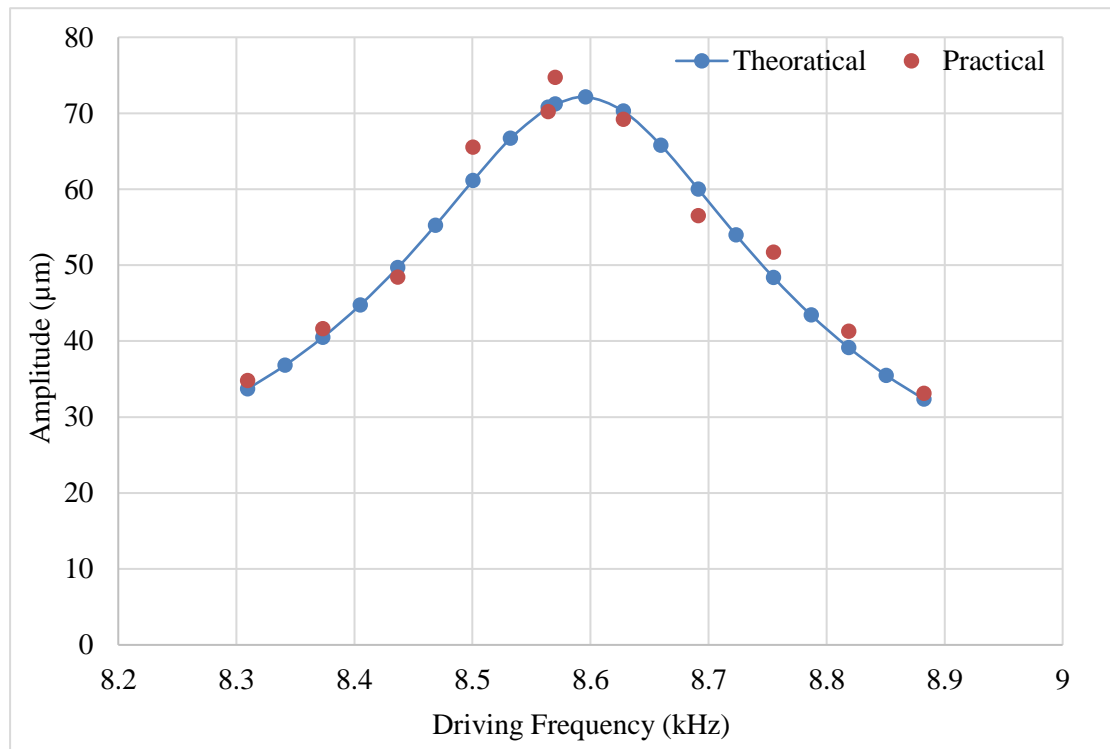


Figure 4.6 Amplitude Vs Driving Frequency in Dynamic Mode

The amplitude of the CMOS-MEMS device increases as the driving frequency reaches to resonance frequency. The amplitude of the CMOS-MEMS device decrease as the driving frequency goes far away from the resonance frequency.

4.1.5 Temperature Vs Piezoresistor (PZR) Resistance:

The calibration curve of the temperature sensor is defined in terms of change in resistance of polysilicon piezoresistors (PZR) change per degree change in temperature. This is necessary to check the temperature of the device while the actuator is placed under the optical microscope when the current inputted. We check the temperature in terms of resistance changes of the PZR. Therefore, it was necessary to define the calibration curve to determine the temperature of the CMOS-MEMS device during experimental characterization. We define the calibration curve before the experimental characterization and analyzed that the resistance vs temperature of

chip behave as linear behavior as shown in fig. 4.7. As the temperature increases or decreases, the resistance of PZR also increases or decreases respectively.

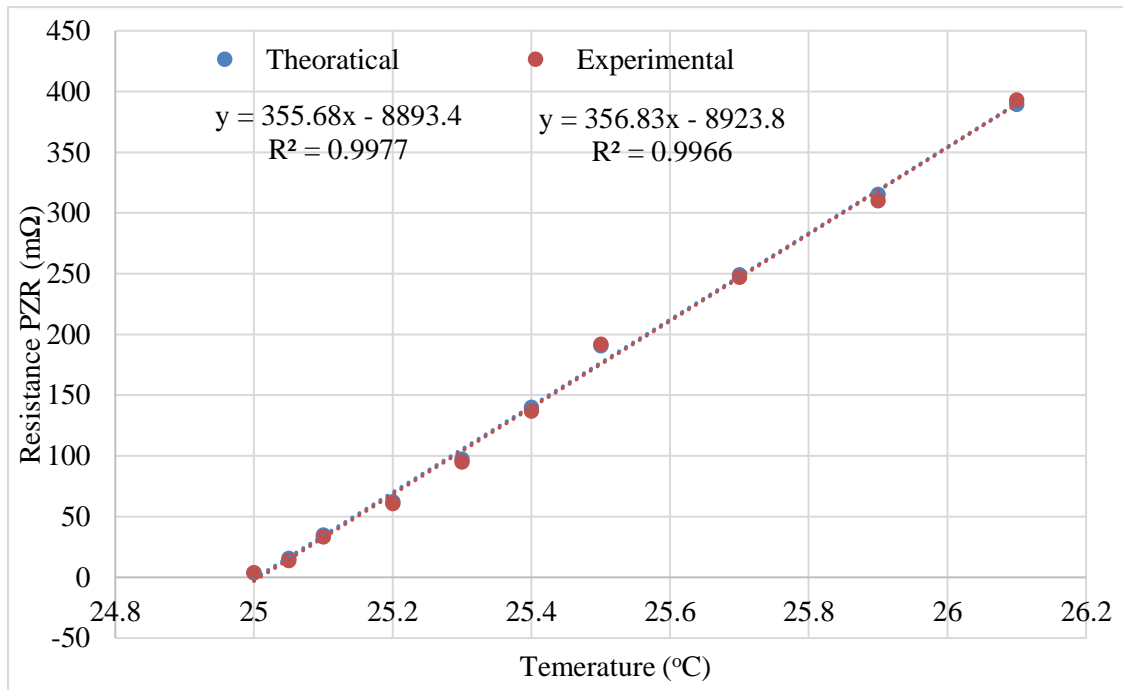


Figure 4.7 Central Shuttle Temperature Vs Resistance Changes in PZR

4.1.6 PZR Resistance Vs Input Current Vs Temperature Rise:

When the input current is applied to the CMOS-MEMS ET actuator, the thermal expansion in the long beams are produce along the change in temperature according to the joule heating effect principle. The resistance in PZR at the end of long beams changes as the temperature changes. This combine effect of change in temperature and change in PZR resistance relative to the input current is shown in fig. 4.8.

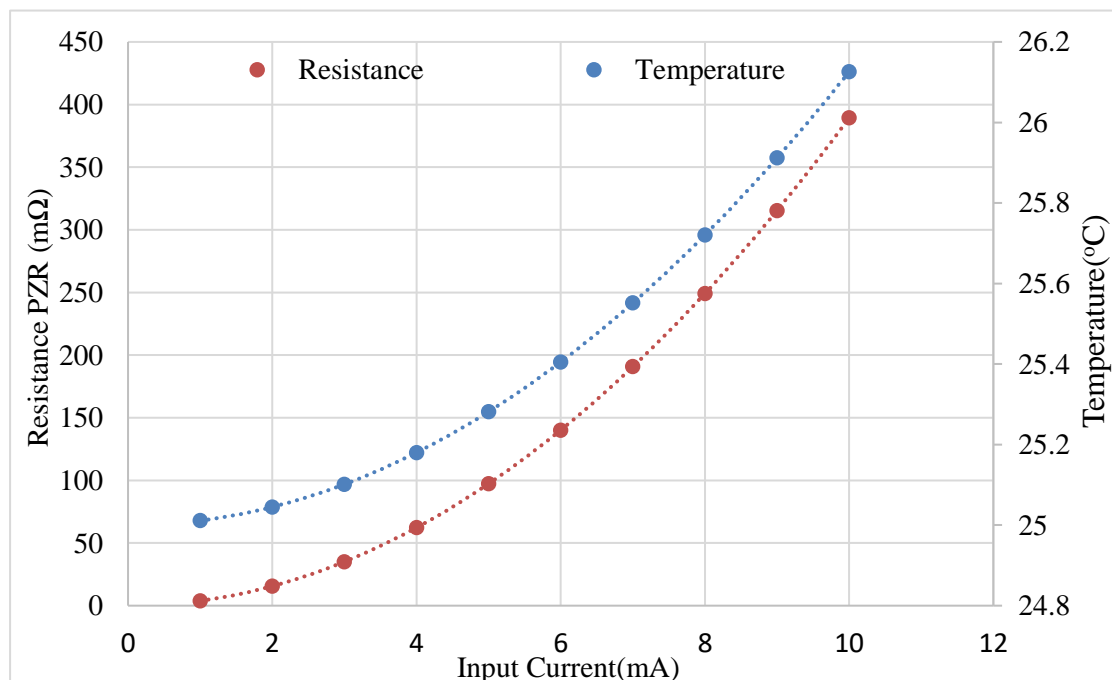


Figure 4.8 Resistance Change in PZR Vs Input Current Vs Temperature Changes in Central Shuttle

4.2 Discussions:

Theoretical analysis has been performed on MATLAB and compared to the experimental analysis which is performed by optical characterization method. It has been recorded that theoretical analysis is very close to the experimental analysis. There is small difference between these two analyses which is reported in table. 4.1

Table 4.1 Comparison between Experimental and Theoretical Analysis

Sr.#	Parameter	Experimental	Theoretical	Percentage Difference
01	Resonance Frequency	8570Hz	8596Hz	0.3%
02	Amplitude	74.5 μm	72.15 μm	3%
03	Quality factor	30.07	29.16	3%
04	Damping Ratio	0.0170	0.0171	0.5%
05	Sensitivity	508nm/mA	494nm/mA	2.7%
06	Thermal Force	686nN/mA	668nN/mA	2.6%
07	PZR Resistance	356 $\text{m}\Omega/^{\circ}\text{C}$	355 $\text{m}\Omega/^{\circ}\text{C}$	0.28%

The 0.3% difference in the resonance frequency is due to the presence of minute Si underneath CMOS layers during the micro fabrication process. There is very difficult to control the thickness of the Si underneath shuttle CMOS layers during the micro fabrication of MPW chip. Therefore, up to 5% variation between the experimental and theoretical measurement are normal [47].

Initially, the temperature of the CMOS-MEMS ET actuator is at room temperature i.e. 25 $^{\circ}\text{C}$ when no current passes through long beams. The temperature is produced as the input current is applied. As the input current increases, temperature increases in exponential form due to the presence of previous input current temperature as shown in fig.4.1.

When the input current passes through the long beams, thermal expansion is produced in the long beams, displacement is produced finally. The displacement of the shuttle changes as the input current changes. The linear behavior is shown in fig. 4.3 theoretically and experimentally. The shuttle displacement increases as the input current increases linearly. The maximum displacement of the central shuttle is reported to be 5 μm at 10mA experimentally while 4.94 μm at 10mA theoretically in static mode. Further the sensitivity of the central shuttle in terms of nm/mA is described.

The output thermal force increases linearly as the input current changes. The maximum output thermal force is reported to be $6.8\mu\text{N}$ at 10mA input current experimentally while $6.6\mu\text{N}$ at 10mA theoretically as shown in fig. 4.4.

The maximum amplitude is measured $72.15\mu\text{m}$ at resonance frequency 8596Hz , the bandwidth of 295.74Hz , f_1 is 8444.38Hz and f_2 is 8740.12Hz , the quality factor of 29.16 with damping ratio of 0.0171 theoretically at 5mA input current. But the maximum amplitude is measured $74.7\mu\text{m}$ at resonance frequency 8570Hz , the bandwidth of 285Hz , f_1 is 8452Hz and f_2 is 8737Hz , the quality factor of 30.07 with damping ratio of 0.0170 experimentally which is measured via 3dB method from fig.4.6.

The calibration curve is obtained in term of change in PZR resistance per degree change in temperature as shown in fig.4.7. The change in resistance in PZR is linearly changes as the device temperature changes. The maximum change in resistance in PZR is reported to be $393\text{m}\Omega$ at 26.1°C temperature in this device experimentally while $389.3\text{m}\Omega$ at 26.1°C theoretically.

Finally, the combined effect of the PZR resistance change with the change in temperature at input current applied to the CMOS-MEMS ET actuator is shown in fig.4.8. This combine graph tells us that at what the exact value of change in temperature in CMOS-MEMS device and change in PZR resistance at specific input current.

Chapter 5

Conclusion and Future Directions

5.1 Conclusion:

The characterization of electro-thermal (ET) actuator has been presented in this research work. The characterization has been performed by optical method using Olympus BX51M optical microscope to avoid the interference of electromagnetic signal and compared to the theoretical analysis which is performed by MATLAB. The maximum amplitude of this device is measured $74.7\mu\text{m}$ at 8570Hz resonance frequency with quality factor 30.07 experimentally and compared to theoretical measurements which is $72.15\mu\text{m}$ at 8596Hz resonance frequency with quality factor 29.16 at 5mA input current. It is also recorded that the temperature of this device rises gradually in exponential form as increase the current in mA . The sensitivity of the device is measured to be $508.5\text{nm}/\text{mA}$ experimentally and compared to theoretical analysis which is $494.8\text{nm}/\text{mA}$. The shuttle displacement increases as the input current increases linearly. The maximum displacement of the central shuttle is reported to be $5\mu\text{m}$ at 10mA in static mode experimentally. The thermal output force is also measured $686\text{nN}/\text{mA}$ experimentally and compared to the theoretical measurement which is $668\text{nN}/\text{mA}$. The thermal output force is linearly changes as the input current changes. The maximum output thermal force is reported to be $6.8\mu\text{N}$ at 10mA input current experimentally. Further, calibration curve of the temperature sensor is defined to calculate the sensitivity of PZR. The sensitivity of the PZR is measured in terms of change in resistance in PZR per degree change in temperature ($\Omega/^{\circ}\text{C}$) in the CMOS-MEMS chip. The sensitivity is measured when temperature in the central shuttle changes as the input current changes which effects on the change in resistance in PZR. The change in resistance in PZR is measured to be $356\text{m}\Omega/^{\circ}\text{C}$ experimentally and compared to the theoretical measurement which is $355\text{m}\Omega/^{\circ}\text{C}$. The change in resistance in PZR is linearly changes as the device temperature changes. The maximum change in resistance is reported to be $393\text{m}\Omega$ at 26.1°C temperature in this device experimentally. A combine effect of the change in

resistance in PZR and change in temperature at input current is also measured to evaluate the change in temperature as well as PZR resistance at specific input current in the chip.

5.2 Future Work:

The CMOS-MEMS ET actuator has been used to determine the displacement or amplitude by optical method in this research work. Another effective method may also be used to determine the displacement or amplitude of the actuator. The capacitance effect may produce among the stator fingers and resonating central shuttle fingers. The capacitance may change among the fingers of the resonating shuttle and the stator fingers during shuttle vibrations. Thus the actuator displacement of amplitude may determine with the help of change in capacitance among the fingers of shuttle and stator part of chip in future.

References

- [1] E. Mastropaolo, G. S. Wood, I. Gual, P. Parmiter, and R. Cheung, "Electrothermally actuated silicon carbide tunable MEMS resonators," *J. Microelectromechanical Syst.*, vol. 21, no. 4, pp. 811–821, 2012.
- [2] A. Jafarpour and H. B. Ghavifekr, "A Novel MEMS Enabled μ Electro-Thermally Actuated Frequency Tunable Microstrip Patch Antenna," *25th Iran. Conf. Electr. Eng. (ICEE20 17)*, pp. 426–430, 2017.
- [3] S. Banerji, D. Fernandez, and J. Madrenas, "Characterization of CMOS-MEMS Resonant Pressure Sensors," *IEEE Sens. J.*, vol. 17, no. 15 October, 2017, pp. 6653–6661, 2017.
- [4] P. J. Gilgunn, J. Liu, N. Sarkar, and G. K. Fedder, "CMOS-MEMS Lateral Electrothermal Actuators," *J. Microelectromechanical Syst.*, vol. 17, no. 1, pp. 103–114, 2008.
- [5] Y. Y. Feng, S. J. Chen, and P. H. Hsieh, "Fabrication of an Electro-Thermal Micro Gripper Using Silver-Nickel Ink," *Proc. IEEE Int. Conf. Micro Electro Mech. Syst.*, no. J24–28 January 2016, pp. 1141–1144, 2016.
- [6] D. S. Chen *et al.*, "An Electrothermal actuator with two degrees of freedom serving as the arm of a MEMS gripper," *IEEE Trans. Ind. Electron.*, vol. 61, no. 10, pp. 5465–5471, 2014.
- [7] W. Wang, Q. Chen, D. Wang, L. Zhou, and H. Xie, "A bi-directional large-stroke electrothermal MEMS mirror with minimal thermal and temporal drift," *Proc. IEEE Int. Conf. Micro Electro Mech. Syst.*, no. 22-26 January, 2017, pp. 331–334, 2017.
- [8] T. Dhakshina Moorthy and P. Nair, "Modeling 3-dimensional electro thermal actuation of MEMS mirrors," *2017 Int. Conf. Nextgen Electron. Technol. Silicon to Software, ICNETS2 2017*, no. 4, pp. 117–121, 2017.

- [9] E. Bertarelli, A. Colnago, R. Ardito, G. Dubini, and A. Corigliano, “Modelling and characterization of circular microplate electrostatic actuators for micropump applications,” *2015 16th Int. Conf. Therm. Mech. Multi-Physics Simul. Exp. Microelectron. Microsystems*, pp. 1–7, 2015.
- [10] E. Brusa, G. De Pasquale, and A. Somà, “Experimental characterization of electro-thermo-mechanical coupling in gold RF microswitches,” *J. Microelectromechanical Syst.*, vol. 22, no. 4 August, 2013, pp. 919–929, 2013.
- [11] F. Han, W. Wang, X. Zhang, and H. Xie, “Modeling and control of a large-stroke electrothermal MEMS mirror for fourier transform microspectrometers,” *J. Microelectromechanical Syst.*, vol. 25, no. 4 August, pp. 750–760, 2016.
- [12] Vikram Mukundan, Pierre Ponce, H. E. Butterfield, and B. L. Pruitt, “Modeling and Characterization of Electrostatic Comb-drive Actuators in Conducting Liquid Media,” *J. Micromechanics Microengineering.*, vol. 19, no. 6, pp. 1–9, 2010.
- [13] J. Varona, M. Tecpoyotl-Torres, J. Escobedo-Alatorre, and A. A. Hamoui, “Design and fabrication of a MEMS thermal actuator for 3D optical switching applications,” *LEOS Summer Top. Meet.*, pp. 31–32, 2008.
- [14] R. C. Voicu, C. Tibeica, R. Muller, and A. Dinescu, “An SU-8 micro-tweezer based on the chevron electro-thermal actuators with a large in-plane displacement,” *Proc. Int. Semicond. Conf. CAS*, vol. October, 2, pp. 105–108, 2017.
- [15] X. Zhang, L. Liu, W. Liang, X. Li, and H. Xie, “An electrothermal/electrostatic dual driven MEMS scanner with large in-plane and out-of-plane displacement,” *Int. Conf. Opt. MEMS Nanophotonics*, no. August, pp. 13–14, 2013.
- [16] M. H. Hristov, T. B. Takov, I. N. Cholakova, K. H. Denishev, V. E. Grozdanov, and D. G. Gaydazhiev, “DESIGN AND INVESTIGATION OF A THERMAL ACTUATOR,” *ELECTRONICS*, no. 09-2008, pp. 43–48, 2008.
- [17] K. S. Member *et al.*, “Hybrid Dynamic Modeling of V-Shaped Thermal Micro-Actuators,” *2016 17th Int. Conf. Therm. Mech. Multi-Physics Simul. Exp. Microelectron. Microsystems*, pp. 5–8, 2016.

- [18] Z. Zhang, Y. Yu, X. Liu, and X. Zhang, "Dynamic modelling and analysis of V- and Z-shaped electrothermal microactuators," *Microsyst. Technol.*, vol. 23, no. 8, pp. 3775–3789, 2017.
- [19] C. Lee, "A MEMS VOA using electrothermal actuators," *J. Light. Technol.*, vol. 25, no. 2, pp. 490–498, 2007.
- [20] Y. Zhu, a. Bazaei, S. O. R. Moheimani, and M. R. Yuce, "A Micromachined Nanopositioner With On-Chip Electrothermal Actuation and Sensing," *IEEE Electron Device Lett.*, vol. 31, no. 10, pp. 1161–1163, 2010.
- [21] J. Reinke, G. K. Fedder, and T. Mukherjee, "CMOS-MEMS variable capacitors using electrothermal actuation," *J. Microelectromechanical Syst.*, vol. 19, no. 5, pp. 1105–1115, 2010.
- [22] D. Girbau, M. A. Llamas, J. Casals-Terré, X. Simó-Selvas, L. Pradell, and A. Lázaro, "A low-power-consumption out-of-plane electrothermal actuator," *J. Microelectromechanical Syst.*, vol. 16, no. 3, pp. 719–727, 2007.
- [23] C. M. Chang, S. Y. Wang, R. Chen, J. Andrew Yeh, and M. T. Hou, "A comb-drive actuator driven by capacitively-coupled-power," *Sensors (Switzerland)*, vol. 12, no. 8, pp. 10881–10889, 2012.
- [24] G. Tibi, E. Sachyani, M. Layani, S. Magdassi, and A. Degani, "Analytic modeling and experiments of tri-layer, electro-thermal actuators for thin and soft robotics," *Proc. - IEEE Int. Conf. Robot. Autom.*, pp. 6712–6717, 2017.
- [25] B. Piriyanont, S. O. R. Moheimani, and A. Bazaei, "Design and control of a MEMS micro-gripper with integrated electro-thermal force sensor," *2013 IEEE/ASME Int. Conf. Adv. Intell. Mechatronics Wollongong, Aust.*, no. 9–12July,2013, pp. 479–484, 2013.
- [26] W. Zhang, Y. Zou, T. Lin, F. S. Chau, and G. Zhou, "Development of Miniature Camera Module Integrated With Solid Tunable Lens Driven by MEMS-Thermal Actuator," *J. MICROELECTROMECHANICAL Syst.*, no. November, pp. 1–11, 2016.
- [27] X. Li, Y. Zhao, and T. Hu, "Design of a novel electrothermal actuator for integrated MEMS safety-and-arwing devices," *2015 IEEE 10th Int. Conf.*

- Nano/Micro Eng. Mol. Syst.*, pp. 63–66, 2015.
- [28] D. Girbau, L. Pradell, A. Lázaro, and À. Nebot, “Electrothermally actuated RF MEMS switches suspended on a low-resistivity substrate,” *J. Microelectromechanical Syst.*, vol. 16, no. 5, pp. 1061–1070, 2007.
- [29] M. Rakotondrabe, A. G. Fowler, and S. O. R. Moheimani, “Control of a novel 2-DoF MEMS nanopositioner with electrothermal actuation and sensing,” *IEEE Trans. Control Syst. Technol.*, vol. 22, no. 4, pp. 1486–1497, 2014.
- [30] W. Wang, S. R. Samuelson, J. Chen, and H. Xie, “Miniaturizing fourier transform spectrometer with an electrothermal micromirror,” *IEEE Photonics Technol. Lett.*, vol. 27, no. 13, pp. 1418–1421, 2015.
- [31] J. Varona, M. Tecpoyotl-Torres, and A. A. Hamoui, “Modeling of MEMS thermal actuation with external heat source,” *Electron. Robot. Automot. Mech. Conf. CERMA 2007 - Proc.*, pp. 591–596, 2007.
- [32] D. O. Popa, Byoung Hun Kang, J. T. Wen, H. E. Stephanou, G. Skidmore, and A. Geisberger, “Dynamic modeling and input shaping of thermal bimorph MEMS actuators,” *2003 IEEE Int. Conf. Robot. Autom. (Cat. No.03CH37422)*, vol. 1, pp. 1470–1475, 2003.
- [33] J. J. Khazaai and H. Qu, “Electro-thermal MEMS switch with latching mechanism: Design and characterization,” *IEEE Sens. J.*, vol. 12, no. 9, pp. 2830–2838, 2012.
- [34] Z. Zhang, Y. Yu, X. Liu, and X. Zhang, “Dynamic electro-thermal modeling of V- and Z-shaped electrothermal microactuator,” *2016 IEEE Int. Conf. Mechatronics Autom. IEEE ICMA 2016*, pp. 890–895, 2016.
- [35] Guan Changhong and Y. Zhu, “An electrothermal microactuator with Z-shaped beams,” *J. Micromechanics Microengineering*, vol. 2, no. August 2016, pp. 81–82, 2010.
- [36] F. Ahmad, J. O. Dennis, N. H. Hamid, and M. H. M. Khir, “Micro Paddle Bridge Resonator for Magnetic Field Measurements,” *Saudi Int. Electron. Commun. Photonics Conf.*, no. 23–26 April, 2011.
- [37] F. Ahmad, J. O. Dennis, M. H. B. M. Khir, N. H. Bin Hamid, and A. Yar,

- “Modeling and simulation of two modes of vibration in MEMS devices based on embedded piezoresistors,” *2014 5th Int. Conf. Intell. Adv. Syst. Technol. Conver. Sustain. Futur. ICIAS 2014 - Proc.*, 2014.
- [38] J. O. Dennis, F. Ahmad, M. H. B. M. Khir, and N. H. Bin Hamid, “Post micromachining of MPW based CMOS–MEMS comb resonator and its mechanical and thermal characterization,” *Microsyst. Technol.*, vol. 22, no. 12, pp. 2909–2919, 2016.
- [39] I. Farooq Ahmad, Member, IEEE, John Ojur Dennis, Member and M. H. M. K. and N. H. Hamid, “Modeling and Layout Design of Resonant Lateral Comb Magnetic Sensor,” *Sensors Transducers J.*, vol. 07, no. December 2012, pp. 1–12, 2012.
- [40] M. Tecpoyotl-Torres, J. Varona, A. A. Hamoui, J. Ecobedo-Alatorre, and J. Sanchez-Mondragón, “Polysilicon thermal microactuators for heat scavenging and power conversion,” *J. Micro/Nanolithography, MEMS, MOEMS*, vol. 8, no. 2, 2009.
- [41] H. Guo and H. Zhang, “Novel Electro-Thermal Actuated Micro Position Lock,” *Proceedings. 7th Int. Conf. Solid-State Integr. Circuits Technol. 2004.*, no. 8–21 Oct. 2004, pp. 1915–1918, 2004.
- [42] J. O. Dennis, A. Y. Ahmed, M. H. Md. Khir, and A. A. S. Rabih, “Modelling and simulation of the effect of air damping on the frequency and quality factor of a CMOS-MEMS resonator,” *Appl. Math. Inf. Sci.*, vol. 9, no. 2, pp. 729–737, 2015.
- [43] J. O. Dennis, F. Ahmad, H. Bin Md Khir, and N. H. Bin Hamid, “Optical characterization of lorentz force based CMOS-MEMS magnetic field sensor,” *Sensors (Switzerland)*, vol. 15, no. 8, pp. 18256–18269, 2015.
- [44] F. Ahmad, J. O. Dennis, N. H. Hamid, and M. H. M. Khir, “Design and Simulation of Mechanical Behavior of MEMS-based Resonant Magnetic Field Sensor with Piezoresistive,” *2nd Int. Conf. Mech. Electr. Technol.*, no. 10–12 Sept. 2010, pp. 584–587, 2010.
- [45] F. Ahmad, J. O. Dennis, M. H. M. Khir, and N. H. Hamid, “Modeling and

- Microfabrication of a CMOS Resonator for Magnetic Field Measurement,” *2012 4th Int. Conf. Intell. Adv. Syst. A Conf. World Eng. Sci. Technol. Congr.*, vol. 2, no. 12–14 June 2012, pp. 701–706, 2012.
- [46] A.Y.Ahmad, Dennis, J.O., H. H. M. Khir, and M. N. Mohamad Saad, “Design and characterization of embedded microheater on CMOS-MEMS resonator for application in mass-sensitive gas sensors,” *5th Int. Conf. Intell. Adv. Syst. (ICIAS)*, no. 3–5 June 2014, 2014.
- [47] F. Ahmad, J. O. Dennis, M. H. M. Khir, N. H. Hamid, and A. Yar, “A new technique to measure the thickness of micromachined structures using an optical microscope,” *3rd Int. Conf. Fundam. Appl. Sci. (ICFAS 2014)*, no. 3–5 June 2014, pp. 650–656, 2014.

Appendix I

Analytical Calculations:

$$i = i_{x1} + i_{x2}$$

$$i_{x1} = i_{x2}$$

$$i_{x1} = i_{x1M1} + i_{x1M2} + i_{x1M3}$$

$$i_{x2} = i_{x2M1} + i_{x2M2} + i_{x2M3}$$

$$F_T = \frac{Ewt^3 d_l}{4l^3}$$

$$d_l = [l^2 + 2(l)\Delta l - l \cos(\alpha)^2]^{\frac{1}{2}} - l \sin(\alpha)$$

$$t_{\max(x=l/2)} = t_{amb} + \frac{1}{2k_e} \frac{v_a^2 A_{m2} (l/2)^2}{\rho_e l V}$$

$$\ddot{Z} + \gamma \dot{Z} + \omega^2 Z = \frac{F_o}{m} e^{j\omega_d t}$$

$$Y = \mathcal{Re}\{Z\}$$

$$Y = \mathcal{Re}\left\{\ddot{Z} + \gamma \dot{Z} + \omega^2 Z = \frac{F_o}{m} e^{j\omega_d t}\right\}$$

$$Y = m\ddot{Y} + b\dot{Y} + kY = F_T \cos\omega_d t$$

$$Y_{SS}(t) = A \cos\omega_d t + B \sin\omega_d t$$

$$Y_{SS}(t) = \frac{d(Y_{SS}(t))}{dt} = -\omega_d A \sin\omega_d t + \omega_d B \cos\omega_d t$$

$$Y_{SS}(t) = \frac{d^2(Y_{SS}(t))}{dt^2} = -\omega_d^2 A \cos\omega_d t - \omega_d^2 B \sin\omega_d t$$

Substituting the values of $\ddot{X}_{SS}(t)$, $\dot{X}_{SS}(t)$, and $X_{SS}(t)$ in above Eq.

$$m(-\omega_d^2 A \cos\omega_d t - \omega_d^2 B \sin\omega_d t) + b(-\omega_d A \sin\omega_d t + \omega_d B \cos\omega_d t) + k(A \cos\omega_d t + B \sin\omega_d t) = F_T \cos\omega_d t$$

$$(-\omega_d^2 mA + \omega_d bB + kA) \cos\omega_d t + (-\omega_d^2 mB - \omega_d bA + kB) \sin\omega_d t = F_T \cos\omega_d t$$

Comparing coefficient of $\cos\omega_d t$ and $\sin\omega_d t$, we get:

$$-\omega_d^2 mA + \omega_d bB + kA = F_T$$

$$-\omega_d^2 mB - \omega_d bA + kB = 0$$

By substituting following in above two system of equation:

$$\omega_0 = \sqrt{\frac{k}{m}} \quad \text{and} \quad \gamma = \frac{b}{m}$$

Solution of system of linear equation is:

$$A = \frac{\frac{F_T}{m}(\omega_0^2 - \omega_d^2)}{(\omega_0^2 - \omega_d^2)^2 + (\gamma\omega_d)^2}, \quad B = \frac{\frac{F_T}{m}(\gamma\omega_d)}{(\omega_0^2 - \omega_d^2)^2 + (\gamma\omega_d)^2}$$

Thus the steady state solution of non-homogeneous 2nd order differential equation is obtained as:

$$Y_{ss} = \left\{ \frac{\frac{F_T}{m}(\omega_0^2 - \omega_d^2)}{(\omega_0^2 - \omega_d^2)^2 + (\gamma\omega_d)^2} \right\} \cos\omega_d t + \left\{ \frac{\frac{F_T}{m}(\gamma\omega_d)}{(\omega_0^2 - \omega_d^2)^2 + (\gamma\omega_d)^2} \right\} \sin\omega_d t$$

$$\nabla A = \sqrt{A^2 + B^2}$$

$$\nabla A = \sqrt{\left[\frac{\frac{F_T}{m}(\omega_0^2 - \omega_d^2)}{(\omega_0^2 - \omega_d^2)^2 + (\gamma\omega_d)^2} \right]^2 + \left[\frac{\frac{F_T}{m}(\gamma\omega_d)}{(\omega_0^2 - \omega_d^2)^2 + (\gamma\omega_d)^2} \right]^2}$$

$$\nabla A = \sqrt{\frac{\left(\frac{F_T}{m}\right)^2 [(\omega_0^2 - \omega_d^2)^2 + (\gamma\omega_d)^2]}{[(\omega_0^2 - \omega_d^2)^2 + (\gamma\omega_d)^2]^2}}$$

$$\nabla A = \frac{F_T/m}{\sqrt{(\omega_0^2 - \omega_d^2)^2 + (\gamma\omega_d)^2}} \quad \text{where} \quad F_T = \frac{Ewt^3 d_l}{4l^3}$$

Thus the output differential amplitude (∇A) is:

$$\nabla A = \frac{\left(\frac{Ewt^3 d_l}{4l^3}\right) / m}{\sqrt{(\omega_0^2 - \omega_d^2)^2 + (\gamma\omega_d)^2}}$$

$$\gamma = 2\xi\omega_0 = \frac{b}{m}$$

$$\nabla A_{max} = \frac{F_T}{m\omega_0\gamma}$$

$$\nabla A_{max} = \frac{\left(\frac{Ewt^3 d_l}{4l^3}\right)}{m\omega_0\gamma}$$

$$\tan\delta = \frac{B}{A} = \frac{\left(\frac{\frac{F_o}{m} (\gamma\omega_d)}{(\omega_o^2 - \omega_d^2)^2 + (\gamma\omega_d)^2} \right)}{\left(\frac{\frac{F_o}{m} (\omega_o^2 - \omega_d^2)}{(\omega_o^2 - \omega_d^2)^2 + (\gamma\omega_d)^2} \right)}$$

$$\tan\delta = \frac{\gamma\omega_d}{\omega_o^2 - \omega_d^2}$$

$$\delta = \tan^{-1} \left(\frac{\gamma\omega_d}{\omega_o^2 - \omega_d^2} \right)$$

$$\xi = \frac{\gamma}{2\omega_o} = \frac{1}{2Q} = \frac{b}{2m\omega_o} = \frac{b}{b_c} \quad \text{Where } b_c = 2\sqrt{km}$$

$$Q = \frac{\omega_o}{\gamma} = \frac{f_r}{\Delta f_{3dB}} = \frac{m\omega_o}{b} = \frac{1}{2\xi}$$

$$F_1 = \mu \frac{A_p}{d_p} \dot{x} = C_1 \dot{x}$$

$$F_2 = \mu \frac{A_p}{\delta} \dot{x} = C_2 \dot{x} \quad \text{Where } \delta = \sqrt{2\mu/\rho_{air}w}$$

$$F_3 = \mu \frac{A_p}{d_s} \dot{x} = C_3 \dot{x}$$

$$F = F_1 + F_2 + F_3$$

$$F = \mu \frac{A_p}{d_p} \dot{x} + \mu \frac{A_p}{\delta} \dot{x} + \mu \frac{A_p}{d_s} \dot{x}$$

$$F = C_1 \dot{x} + C_2 \dot{x} + C_3 \dot{x}$$

$$F = (C_1 + C_2 + C_3) \dot{x}$$

$$k_b = \frac{F}{Y_{dis}} = \frac{12EI}{l^3} = \frac{Ewt^3}{l^3} \quad \text{Where } I = \frac{1}{12}wt^3$$

$$k_y = Nk_b = N \frac{Ewt^3}{l^3}$$

$$f = \frac{1}{T} = \frac{\omega_o}{2\pi}$$

$$f_r = \frac{1}{2\pi} \sqrt{\frac{k}{m}}$$

$$f_r = \frac{1}{2\pi} \sqrt{\frac{4 \left(\frac{Ewt^3}{l^3} \right)}{\rho_{av}(V_s + V_b)}}$$

$$\rho_{av} = \frac{\rho_{Si} \times t_{Si} + \rho_{SiO_2} \times t_{SiO_2} + \rho_{Al} \times t_{Al}}{t_{Si} \times t_{SiO_2} \times t_{Al}}$$

$$R = \rho \frac{l}{A}$$

$$R(t) = R_o \{1 + \alpha(t - t_o)\}$$

Appendix II

MATLAB CODE for Resonance Frequency and Quality Factor:

```
%%Charaterization of on Chip CMOS-MEMS Eletro-thermal (ET) Actuator
```

```
%% Perameter Initialization in micron
```

```
dl=755*10^(-6); % Length of Device
dw=680*10^(-6); % Width of Device
lb=300*10^(-6); % Long beams Length
wb=3*10^(-6); % Long beams width
tb=4.5*10^(-6); % Long beams thickness
lshuttle=155*10^(-6); % shuttle Length
wshuttle=100*10^(-6); % shuttle Width
tshuttle=4.5*10^(-6); % shuttle thickness
lfinger=60*10^(-6); % shuttle Fingers length
wfinger=3*10^(-6); % shuttle Fingers width
tfinger=4.5*10^(-6); % shuttle Fingers thickness
lstator_fing=60*10^(-6); % stator Fingers length
wstator_fing=3*10^(-6); % stator Fingers width
tstator_fing=4.5*10^(-6); % stator Fingers thickness
Aetch_hole=10*10*10^(-12); % Area of etched hole
mshuttle=541.29*(10^(-12)); % Mass of shuttle
```

```
%% Material Properties
```

```
E_SiO2=73*10^9; %Youngs Modulus of Silicon dioxide
E_Si=130*10^9; %Youngs Modulus of Silicon
E_Al=77*10^9; %Youngs Modulus of Aluminum
E_Sipoly=169*10^9; %Youngs Modulus of Poly Silicon
P_SiO2=2648; %Density of Silicon dioxide
P_Si=2328; %Density of Silicon
P_Al=2700; %Density of Aluminum
P_Sipoly=2300; %Density of Poly Silicon
```

```
%% Material Thickness with Silicon Substrate
```

```
tSi=60*10^(-6); %Thickness of Si
tSiO2=0.710*10^(-6); %Thickness of SiO2
tAl1=0.624*10^(-6); %Thckness of Metal 1 Layers
tAl2=0.612*10^(-6); %Thickness of Metal 2 Layers
tAl3=0.877*10^(-6); %Thickness of Metal 3 Layers
tAl=tAl1+tAl2+tAl3 %Thickness of all three Al Layers
tM1_M2=0.720*10^(-6); %Dielectric Thickness from M1 to M2
tM2_M3=0.660*10^(-6); %Dielectric Thickness from M2 to M3
tPoly=0.285*10^(-6)
t_T=tSi+tSiO2+tAl+tM1_M2+tM2_M3+tPoly; %Total thickness With Silicon
```

```
%% Spring Constant or Stiffness
```

```
E=(E_Al+E_SiO2)/2 % Average of Youngs Modulus of Aluminum and Polysilicon
N=4; % total numbers of beams
ky=N*((E*tb*(wb)^3)/(lb)^3)
```



```

%% Shuttle Volume
l_rod=310*10^(-6);           %Length of upper rod
w_rod=30*10^(-6);           %Width of lower rod
Area_rod1=l_rod*w_rod;       %Upper Rod Area
Area_rod2=l_rod*w_rod;       %Lower Rod Area
C_lshuttle=155*10^(-6);     %Central Shutte Length
C_wshuttle=100*10^(-6);     %Central Shuttle Width
C_area=C_lshuttle*C_wshuttle; %Central Shuttle Area
tAetch_hole=86*Aetch_hole;   %Total area of 86 holes
Net_area_rotor=(Area_rod1+C_area+Area_rod2)-(tAetch_hole);
                                %Net area of Rotor Part
Vol_rotor=Net_area_rotor*tshuttle; %Volume of Rotor without finger
Vol_finger=lfinger*wfinger*tfinger; %Volume of one finger
Vol_tfingers=52*Vol_finger;      %Volume of 52 fingers
Vol_shuttle=Vol_rotor+Vol_tfingers %Volume of shuttle with fingers

%% Volume of Beams
Vol_beam1=lb*wb*tb;           %Volume of one beam
Vol_beams=4*Vol_beam1

%% Effective Mass
P_average=(P_SiO2+P_Al)/2
M=P_average*(Vol_shuttle+Vol_beams)
m=M*ones(1,10);

%% Resonance Frequency
wn=sqrt(ky/M)                 %Angular Resonance frequency
fr=wn/(2*pi)                 %Resonance Frequency
gema=1852                    %Damping Constant
zeta=gema/(2*wn)
b=gema*M                     %Damping Coefficient
Q=(wn)/gema                  %Quality Factor

```

MATLAB CODE for Damping and Damping Ratio:

```

%% Damping and Damping Ratio

%% Parameter Initialization in micron
dl=755*10^(-6);           % Length of Device
dw=680*10^(-6);           % Width of Device
lb=300*10^(-6);           % Long beams Length
wb=3*10^(-6);             % Long beams width
tb=4.5*10^(-6);           % Long beams thickness
lshuttle=155*10^(-6);     % shuttle Length
wshuttle=100*10^(-6);     % shuttle Width
tshuttle=4.5*10^(-6);     % shuttle thickness
lfinger=60*10^(-6);       % shuttle Fingers length
wfinger=3*10^(-6);        % shuttle Fingers width
tfinger=4.5*10^(-6);      % shuttle Fingers thickness
lstator_fing=60*10^(-6);  % stator Fingers length
wstator_fing=3*10^(-6);   % stator Fingers width
tstator_fing=4.5*10^(-6); % stator Fingers thickness
Aetch_hole=10*10*10^(-12); % Area of etched hole
mshuttle=541.29*(10^(-12)); % Mass of shttle

%% Material Properties
E_SiO2=73*10^9;           %Youngs Modulus of Silicon dioxide
E_Si=130*10^9;            %Youngs Modulus of Silicon

```

```

E_Al=77*10^9; %Youngs Modulus of Aluminum
E_Sipoly=169*10^9; %Youngs Modulus of Poly Silicon
P_SiO2=2648; %Density of Silicon dioxide
P_Si=2328; %Density of Silicon
P_Al=2700; %Density of Aluminum
P_Sipoly=2300; %Density of Poly Silicon

%% Material Thickness with Silicon Substrate
tSi=60*10^(-6); %Thickness of Si
tSiO2=0.710*10^(-6); %Thickness of SiO2
tAl1=0.624*10^(-6); %Thckness of Metal 1 Layers
tAl2=0.612*10^(-6); %Thckness of Metal 2 Layers
tAl3=0.877*10^(-6); %Thckness of Metal 3 Layers
tAl=tAl1+tAl2+tAl3 %Thickness of all three Al Layers
tM1_M2=0.720*10^(-6); %Dielectric Thickness from M1 to M2
tM2_M3=0.660*10^(-6); %Dielectric Thickness from M2 to M3
tPoly=0.285*10^(-6)
t_T=tSi+tSiO2+tAl+tM1_M2+tM2_M3+tPoly; %Total thickness With Silicon

%% Spring Constant or Stiffness
E=(E_Al+E_SiO2)/2
% Average of Youngs Modulus of Aluminum and Polysilicon
N=4; % total numbers of beams
ky=N*((E*tb*(wb)^3)/(lb)^3)

%% Shuttle Volume
l_rod=310*10^(-6); %Length of upper rod
w_rod=30*10^(-6); %Width of lower rod
Area_rod1=l_rod*w_rod; %Upper Rod Area
Area_rod2=l_rod*w_rod; %Lower Rod Area
C_lshuttle=155*10^(-6); %Central Shutte Length
C_wshuttle=100*10^(-6); %Central Shuttle Width
C_area=C_lshuttle*C_wshuttle; %Central Shuttle Area
tAetch_hole=86*Aetch_hole; %Total area of 86 holes
Net_area_rotor=(Area_rod1+C_area+Area_rod2)-(tAetch_hole); %Net area of Rotor Part
Vol_rotor=Net_area_rotor*tshuttle; %Volume of Rotor without finger
Vol_finger=lfinger*wfinger*tfinger; %Volume of one finger
Vol_tfingers=52*Vol_finger; %Volume of 52 fingers
Vol_shuttle=Vol_rotor+Vol_tfingers %Volume of shuttle with fingers

%% Volume of Beams
Vol_beam1=lb*wb*tb; %Volume of one beam
Vol_beams=4*Vol_beam1

%% Effective Mass
P_average=(P_SiO2+P_Al)/2
M=P_average*(Vol_shuttle+Vol_beams)
m=M*ones(1,10);

%% Damping Calculation
bc=2*sqrt(ky*M);
wn=sqrt(ky/M);
fr=wn/(2*pi)
eta=18.5*10^(-6);
n1=26+26+27+27;
n=26+26;
lo=30*10^(-6);
xo=30*10^(-6);
d=3*10^(-6);
x=340*10^(-6);

```

```

b=(eta*((0.422*n1*tfinger*(tfinger)^3)/(xo)^3)+((2*n*tfinger*lo)/d)+
((n*lfinger*wfinger)+(4*l_rod*w_rod)+(lshuttle*wshuttle))/x))
gema=b/M
zeta=b/bc

```

MATLAB CODE for Shuttle Displacement and Thermal Force:

```
%%Shuttle Displacement and output Thermal Force
```

```
%% Parameter Initialization in micron
```

```

dl=755*10^(-6);           % Length of Device
dw=680*10^(-6);           % Width of Device
lb=300*10^(-6);           % Long beams Length
wb=3*10^(-6);             % Long beams width
tb=4.5*10^(-6);           % Long beams thickness
lshuttle=155*10^(-6);      % shuttle Length
wshuttle=100*10^(-6);      % shuttle Width
tshuttle=4.5*10^(-6);      % shuttle thickness
lfinger=60*10^(-6);        % shuttle Fingers length
wfinger=3*10^(-6);         % shuttle Fingers width
tfinger=4.5*10^(-6);       % shuttle Fingers thickness
lstator_fing=60*10^(-6);   % stator Fingers length
wstator_fing=3*10^(-6);    % stator Fingers width
tstator_fing=4.5*10^(-6);  % stator Fingers thickness
Aetch_hole=10*10*10^(-12); % Area of etched hole
mshuttle=541.29*(10^(-12)); % Mass of shuttle

```

```
%% Material Properties
```

```

E_SiO2=73*10^9;           %Youngs Modulus of Silicon dioxide
E_Si=130*10^9;            %Youngs Modulus of Silicon
E_Al=77*10^9;             %Youngs Modulus of Aluminum
E_Sipoly=169*10^9;        %Youngs Modulus of Poly Silicon
P_SiO2=2648;              %Density of Silicon dioxide
P_Si=2328;                %Density of Silicon
P_Al=2700;                %Density of Aluminum
P_Sipoly=2300;            %Density of Poly Silicon

```

```
%% Material Thickness with Silicon Substrate
```

```

tSi=60*10^(-6);           %Thickness of Si
tSiO2=0.710*10^(-6);      %Thickness of SiO2
tAl1=0.624*10^(-6);       %Thickness of Metal 1 Layers
tAl2=0.612*10^(-6);       %Thickness of Metal 2 Layers
tAl3=0.877*10^(-6);       %Thickness of Metal 3 Layers
tAl=tAl1+tAl2+tAl3        %Thickness of all three Al Layers
tM1_M2=0.720*10^(-6);     %Dielectric Thickness from M1 to M2
tM2_M3=0.660*10^(-6);     %Dielectric Thickness from M2 to M3
tPoly=0.285*10^(-6)       %Dielectric Thickness of Poly
t_T=tSi+tSiO2+tAl+tM1_M2+tM2_M3+tPoly; %Total thickness With Silicon

```

```
%% Spring Constant or Stiffness
```

```

E=(E_Al+E_SiO2)/2
    % Average of Youngs Modulus of Aluminum and Polysilicon
N=4; % total numbers of beams
ky=N*((E*tb*(wb)^3)/(lb)^3)
%% Thermal Mechanism of Beams
tamb=298.15; %Ambient Temperature in Kelvin
Tamb=tamb*ones(1,10); %Array of Ambient Temperature in Kelvin (1-10)
res=2.87*10^(-8)

```

```

R=173
k=205.0; %thermal conductivity of aluminum W/mK
delT=[];
Tshuttle=[];
for i=0.001:0.001:0.01; % Operating AC Current from 1mA to 10mA;
delT=[delT 4*((i^2).*R)/((lb)*k)]; % Change in Temperature in
Beams
Tshuttle=[Tshuttle
((1/(2*k))*((i^2*res*(lshuttle)^3)/(4*(wshuttle*tAl2)*Vol_shuttle)))]
;
% Change in Temperature in Shuttle
end
T=Tshuttle+delT+Tamb; % Total Temperature with Ambient
T_cel=T-273.15;
i=1:1:10;
figure(1);
subplot(1,1,1);
plot(i,T_cel,'b');
grid on;
xlabel('Input Current (mA)');
ylabel('Change in Temperature in Celcius');
title('Input Current Vs Change in Temperature');
col_header={'i','T'};
xlswrite('data.xlsx',[i(:),T_cel(:)],'sheet1','A2');
xlswrite('data.xlsx',col_header,'sheet1','A1');
alpha=24*10^(-6); %TCR=39*10^(-4) Alpha_SiO2=5.8*10^(-6)
del_lb=(alpha*2*(dl)*(T-Tamb));
a=0
disp=sqrt(((lb)^2)*ones(1,10)+2*(lb)*del_lb-
((lb*cos(a))^2)*ones(1,10))-lb*sin(a) %% Shuttle Displacement
figure(2);
subplot(1,1,1);
plot(i,disp,'b');
grid on;
xlabel('Input Current (mA)');
ylabel('Change in Shuttle Displacement (Micrometers)');
title('Input Current Vs Change in Shuttle Displacement');
col_header={'i','disp'};
xlswrite('data.xlsx',[i(:),disp(:)],'sheet2','A2');
xlswrite('data.xlsx',col_header,'sheet2','A1');

%% Output Thermal Force
f_t=ky*disp
figure(3)
subplot(1,1,1);
plot(i,f_t,'m');
grid on;
xlabel('Input Current');
ylabel('Force (Micro Newtons)');
title('Input Current Vs Force');
col_header={'i','f_t'};
xlswrite('data.xlsx',[i(:),f_t(:)],'sheet3','A2');
xlswrite('data.xlsx',col_header,'sheet3','A1');

```

MATLAB CODE for Maximum Amplitude Vs Driving Frequency:

```

%% Maximum Amplitude Vs Driving Frequency

%% Parameter Initialization in micron
dl=755*10^(-6); % Length of Device
dw=680*10^(-6); % Width of Device
lb=300*10^(-6); % Long beams Length
wb=3*10^(-6); % Long beams width
tb=4.5*10^(-6); % Long beams thickness
lshuttle=155*10^(-6); % shuttle Length
wshuttle=100*10^(-6); % shuttle Width
tshuttle=4.5*10^(-6); % shuttle thickness
lfinger=60*10^(-6); % shuttle Fingers length
wfinger=3*10^(-6); % shuttle Fingers width
tfinger=4.5*10^(-6); % shuttle Fingers thickness
lstator_fing=60*10^(-6); % stator Fingers length
wstator_fing=3*10^(-6); % stator Fingers width
tstator_fing=4.5*10^(-6); % stator Fingers thickness
Aetch_hole=10*10*10^(-12); % Area of etched hole
mshuttle=541.29*(10^(-12)); % Mass of shuttle

%% Material Properties
E_SiO2=73*10^9; %Youngs Modulus of Silicon dioxide
E_Si=130*10^9; %Youngs Modulus of Silicon
E_Al=77*10^9; %Youngs Modulus of Aluminum
E_Sipoly=169*10^9; %Youngs Modulus of Poly Silicon
P_SiO2=2648; %Density of Silicon dioxide
P_Si=2328; %Density of Silicon
P_Al=2700; %Density of Aluminum
P_Sipoly=2300; %Density of Poly Silicon

%% Material Thickness with Silicon Substrate
tSi=60*10^(-6); %Thickness of Si
tSiO2=0.710*10^(-6); %Thickness of SiO2
tAl1=0.624*10^(-6); %Thickness of Metal 1 Layers
tAl2=0.612*10^(-6); %Thickness of Metal 2 Layers
tAl3=0.877*10^(-6); %Thickness of Metal 3 Layers
tAl=tAl1+tAl2+tAl3 %Thickness of all three Al Layers
tM1_M2=0.720*10^(-6); %Dielectric Thickness from M1 to M2
tM2_M3=0.660*10^(-6); %Dielectric Thickness from M2 to M3
tPoly=0.285*10^(-6)
t_T=tSi+tSiO2+tAl+tM1_M2+tM2_M3+tPoly; %Total thickness With Silicon

%% Spring Constant or Stiffness
E=(E_Al+E_SiO2)/2
% Average of Youngs Modulus of Aluminum and Polysilicon
N=4; % total numbers of beams
ky=N*((E*tb*(wb)^3)/(lb)^3)

%% Shuttle Volume
l_rod=310*10^(-6); %Length of upper rod
w_rod=30*10^(-6); %Width of lower rod
Area_rod1=l_rod*w_rod; %Upper Rod Area
Area_rod2=l_rod*w_rod; %Lower Rod Area
C_lshuttle=155*10^(-6); %Central Shuttle Length
C_wshuttle=100*10^(-6); %Central Shuttle Width
C_area=C_lshuttle*C_wshuttle; %Central Shuttle Area

```

```

tAetch_hole=86*Aetch_hole; %Total area of 86 holes
Net_area_rotor=(Area_rod1+C_area+Area_rod2)-(tAetch_hole);
%Net area of Rotor Part
Vol_rotor=Net_area_rotor*tshuttle; %Volume of Rotor without finger
Vol_finger=lfinger*wfinger*tfinger; %Volume of one finger
Vol_tfingers=52*Vol_finger; %Volume of 52 fingers
Vol_shuttle=Vol_rotor+Vol_tfingers %Volume of shuttle with fingers

%% Volume of Beams
Vol_beam1=lb*wb*tb; %Volume of one beam
Vol_beams=4*Vol_beam1

%% Effective Mass
P_average=(P_SiO2+P_Al)/2
M=P_average*(Vol_shuttle+Vol_beams)
m=M*ones(1,10);

%% Resonance Frequency
wn=sqrt(ky/M) %Angular Resonance frequency
fr=wn/(2*pi) %Resonance Frequency
gema=1852 %Damping Constant
zeta=gema/(2*wn)
b=gema*M %Damping Coefficient

Q=(wn)/gema %Quality Factor

%% Thermal Mechanism of Beams
tamb=298.15; %Ambient Temperature in Kelvin
Tamb=tamb*ones(1,10); %Array of Ambient Temperature in Kelvin (1-10)
res=2.87*10^(-8)
R=173
k=205.0; %thermal conductivity of aluminum W/mK
delT=[];
Tshuttle=[];
for i=0.001:0.001:0.01; % Operating AC Current from 1mA to 10mA;
delT=[delT 4*((i^2).*R)/((lb)*k)]; % Change in Temperature in Beams
Tshuttle=[Tshuttle
((1/(2*k))*((i^2*res*(lshuttle)^3)/(4*(wshuttle*tAl2)*Vol_shuttle)))]
; % Change in Temperature in Shuttle
end
T=Tshuttle+delT+Tamb; % Total Temperature with Ambient
T_cel=T-273.15;
i=1:1:10;
figure(1);
subplot(1,1,1);
plot(i,T_cel,'b');
grid on;
xlabel('Input Current (mA)');
ylabel('Change in Temperature in Celcius');
title('Input Current Vs Change in Temperature');
col_header={'i','T'};
xlswrite('data.xlsx',[i(:),T_cel(:)],'sheet1','A2');
xlswrite('data.xlsx',col_header,'sheet1','A1');
alpha=24*10^(-6); %TCR=39*10^(-4) Alpha_SiO2=5.8*10^(-6)
del_lb=(alpha*2*(dl)*(T-Tamb));
a=0
disp=sqrt(((lb)^2)*ones(1,10)+2*(lb)*del_lb-
((lb*cos(a))^2)*ones(1,10))-lb*sin(a)
figure(2);
subplot(1,1,1);

```

```

        plot(i,disp,'b');
        grid on;
xlabel('Input Current (mA)');
ylabel('Change in Shuttle Displacement (Micrometers)');
title('Input Current Vs Change in Shuttle Displacement');
col_header={'i','disp'};
xlswrite('data.xlsx',[i(:),disp(:)],'sheet2','A2');
xlswrite('data.xlsx',col_header,'sheet2','A1');

%% Thermal Force
f_t=ky*disp
figure(3)
subplot(1,1,1);
plot(i,f_t,'m');
grid on;
xlabel('Input Current');
ylabel('Force (Micro Newtons)');
title('Input Current Vs Force');
col_header={'i','f_t'};
xlswrite('data.xlsx',[i(:),f_t(:)],'sheet3','A2');
xlswrite('data.xlsx',col_header,'sheet3','A1');
FT=zeros(1,10);
for x=5:5;
    FT=0;
    FT=f_t(x);
A=[];
f=[];

%% Amplitude at Resonance Frequency
for wd=52210:200:56010;
    f=[f (wd)/(2*pi)];
    A=[A (((FT)/M)/(sqrt(((wn^2-wd^2)^2)+(wd.*gema)^2)))/10^(-6)]];
end
fd=f;
figure(4)
subplot(1,1,1);
plot(fd,A,'b');
hold on;
grid on;
xlabel('Driving Frequency');
ylabel('Amplitude (Micrometers)');
title('Amplitude Vs Frequency');
legend('Amplitude vs Resonance frequency')
col_header={'Driving Frequency','Amplitude'};
xlswrite('data.xlsx',[fd(:),A(:)],'sheet4','A2');
xlswrite('data.xlsx',col_header,'sheet4','A1');
end

```

MATLAB CODE for PZR as Temperature Sensor:

```

%% Piezoresistor as a Temperature Sensor.

amb_t=298.15;
To=amb_t*ones(1,10);
ToC=To-273.15*ones(1,10);
TC=[];
R=[];
Ro=113;
alpha_poly=30.6*10^(-4)

```

```
format long
R=[R Ro*(1*ones(1,10)+alpha_poly.*(T-To))];
delR=R-Ro*ones(1,10)
TC=[TC T-273.15*ones(1,10)]
figure(5)
subplot(1,1,1);
plot(TC,delR,'m');
hold on;
grid on;
xlabel('Temperature in Cecius');
ylabel('Change in Resistance PZR (Ohm)');
title('Temerature Vs Change in Resistance PZR');
col_header={'TC','delR'};
xlswrite('data.xlsx',[TC(:),delR(:)],'sheet5','A2');
xlswrite('data.xlsx',col_header,'sheet5','A1');
```